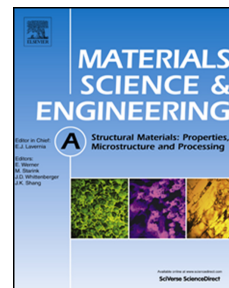


# Journal Pre-proof

Improvement of fracture toughness of Ti+Nb stabilized microalloyed and interstitial free steels processed through single phase regime control multiaxial forging

Sumit Ghosh, Suhrit Mula



PII: S0921-5093(19)31602-8

DOI: <https://doi.org/10.1016/j.msea.2019.138817>

Reference: MSA 138817

To appear in: *Materials Science & Engineering A*

Received Date: 21 September 2019

Revised Date: 11 December 2019

Accepted Date: 11 December 2019

Please cite this article as: S. Ghosh, S. Mula, Improvement of fracture toughness of Ti+Nb stabilized microalloyed and interstitial free steels processed through single phase regime control multiaxial forging, *Materials Science & Engineering A* (2020), doi: <https://doi.org/10.1016/j.msea.2019.138817>.

This is a PDF file of an article that has undergone enhancements after acceptance, such as the addition of a cover page and metadata, and formatting for readability, but it is not yet the definitive version of record. This version will undergo additional copyediting, typesetting and review before it is published in its final form, but we are providing this version to give early visibility of the article. Please note that, during the production process, errors may be discovered which could affect the content, and all legal disclaimers that apply to the journal pertain.

© 2019 Published by Elsevier B.V.

CRedit roles:

1<sup>st</sup> author's contribution: Conceptualization; Data curation; Formal analysis; Investigation; Methodology; Writing - original draft.

2<sup>nd</sup> author's contribution: Validation; Writing - review & editing; Supervision;

## Improvement of fracture toughness of Ti+Nb stabilized microalloyed and interstitial free steels processed through single phase regime control multiaxial forging

Sumit Ghosh<sup>a,b</sup>, Suhrit Mula<sup>a\*</sup>

<sup>a</sup> Department of Metallurgical and Materials Engineering, Indian Institute of Technology, Roorkee-247667, Uttarakhand, India.

<sup>b</sup> Materials and Mechanical Engineering, Centre for Advanced Steels Research, University of Oulu, 90014 Oulun yliopisto, Finland.

\*Corresponding Author: Email: smulafmt@iitr.ac.in, suhritmula@gmail.com

Phone: +91-1332-285763; Fax: +91-1332-285243

### Abstract

Objective of the current study is to enhance the mechanical properties, with a special emphasis on fracture toughness, of Ti+Nb stabilized interstitial free and microalloyed steels through microstructural modification by single-phase controlled multiaxial forging at large cumulative strains. Analysis of fracture toughness was executed through calculating  $K_Q$  (conditional fracture toughness),  $K_{ee}$  (equivalent energy fracture toughness) and  $J$ -integral (crack initiation energy) values from single-edge bend test data of the forged specimens. The effect of strain hardening rate and strain hardening exponent on deformation behavior were examined to correlate the yield strength (YS) and uniform elongation. Also, theoretically calculated YS (obtained from analysis of strengthening mechanisms) was correlated well with the experimentally obtained results. The quantitative measurement of grain size, low- and high-angle grain boundaries and their distribution in the deformed state were investigated through EBSD/TEM analysis. Superior combinations of the YS, ductility (%El.) and fracture toughness were obtained through intercritical ( $\alpha+\gamma$ ) phase regime ( $\sim A_{r1}$ ) control 15 cycles multiaxially forged (MAFed) microalloyed steel (YS=1027MPa, %El.=8.3% and  $K_{ee}$ =90MPa $\sqrt{m}$ ) and pure  $\alpha$ -ferritic region ( $< A_{r1}$ ) control 18 cycles MAFed IF steel (YS=881MPa, %El.=11.2% and  $K_{ee}$ =97MPa $\sqrt{m}$ ) specimens. Enhancement of the fracture toughness is ascertained to the formation of uniformly distributed nanosize fragmented cementite ( $Fe_3C$ ) particles ( $\sim 35nm$  size) within the submicron size ( $\sim 280nm$  size) ferritic microstructure in the microalloyed steel; whereas in case of the IF steel, this is attributed to the formation of ultrafine ferrite grain ( $\sim 320nm$ ) along with dense dislocation substructures. These dislocation cells and fine substructures as well as nanosize  $Fe_3C$

could effectively block the crack initiation and propagation and thereby enhance the fracture toughness.

**Keywords:** Ti+Nb stabilized IF/microalloyed steels; Multiaxial forging; Submicron size ferrite; nanosize fragmented cementite; Fracture toughness; TEM/EBSD analysis.

## 1. Introduction

High yield strength and toughness combination is quite attractive for any structural applications in order to improve both performance and safety as well as weight reduction. Hence, demand of improvement of the mechanical strength of the interstitial free (IF)/microalloyed steels is increased day by day. However, enhancement of the yield strength (YS) without much reducing their ductility and fracture/impact toughness is a challenge. Moreover, grain size refinement through advance processing techniques is one of the effective way by which the fracture toughness as well as strength can be improved simultaneously [1,2]. Among different processing techniques, severe plastic deformation (SPD) technique is the most promising technique to develop bulk size ultrafine grained (UFG) materials, where, the majority of the grain boundaries exhibits high angles of misorientation [3,4]. Several SPD techniques have been extensively exploited to develop UFG materials through different powerful straining methods such as high pressure torsion, equal channel angular extrusion and accumulative roll bonding [5,6]. Till now, as per the available literature, the maximum grain size refinement of IF and low carbon (C) steel is reported to be  $\sim 0.3$  and  $0.2\mu\text{m}$ , respectively, processed by ECAP technique at large equivalent strain of 24 and 17. The maximum improvement of YS is reported to be 895 and 913MPa along with a ductility of 11 and 10.6%, respectively, for IF and low C steels [5,7]. However, expensive tooling are required for most of these techniques, and there is a design difficulties also. Moreover, for some of these techniques, it is tough to obtain bulk size samples with uniform UFG microstructures [8,9].

Among the other SPD techniques, multiaxial forging (MAF) is a unique industrial reliable technique, wherein there is a change in forging path in all three direction (X,Y,Z) alternatively after each pass. Moreover, it can be performed using any conventional forging machine for a broad range of temperatures and strain rates. Numerous mechanisms are anticipated for the manifestation of grain refinement during SPD processes based on the processing conditions and

materials. Lim et al. [10] executed room temperature MAF studies on ferritic Fe-C alloy and achieved fine-grained ferritic structure. The mechanism of grain refinement during multiaxial forging is enlightened through the intersection of microshear bands, which are formed owing to strain localization; and bring about the evolution of subgrains. On further straining, as the subgrain boundaries absorb dislocations, the subgrains transform into grains by rotation, instead of growth [5,10]. Growth process generally occurs when deformation carried out at elevated temperatures, which allows dislocations to both glide and climb [1,2]. However, during multiaxial forging at low temperatures and high strain rate, dislocation movement is more difficult as the subgrains are less mobile [8-10]. Hence, with increase of straining, subgrain boundaries absorb dislocations and subsequently transform into ultrafine grains by rotation, instead of growth [10]. Moreover, deformation induced grain growth in FCC nanocrystalline materials (i.e. Cu, Ni-Fe alloys etc.) at both ambient and cryogenic temperatures have been reported in several literature [11,12]. Wang et al. [11] have observed grain growth during high pressure torsion of Ni-Fe alloy and stated that the rotation of nanosize grains within the shear bands and grain boundary migration are the main mechanisms of grain growth. They have also reported that the grain boundary migration velocity is very sensitive in presence of impurities. Li [12] has observed mechanical grain growth of nanocrystalline Cu at liquid nitrogen temperature, and reported that a high purity and non-equilibrium structures are necessary conditions for the mechanical grain growth. He has demonstrated that the material should be pure enough so that free dislocations are available to move out of the boundary. However, hardly anyone observed the grain coalescence during SPD of BCC materials. Deepa et al. [5] performed ECAP of IF steel at large equivalent strain and observed the formation of deformation bands at low equivalent strain, and with further increase in the strain, the deformation bands split into ribbon-shaped features and finally to the near equiaxed grain structure with subgrains along with high dislocation density. Bhowmik et al. [13] demonstrated that formation of UFG through room temperature MAF of IF steel led to the remarkable increase in the tensile strength with little expense of the ductility. Han et al. [14] conducted multiaxial forging (at 550°C) of austenitic Fe-32 Ni alloy and reported that formation of UFG microstructure is attributed to the continuous dynamic recrystallization. Belyakov et al. [15] studied severe deformation of austenitic stainless steel at 500°C and reported that considerable refinement of initial microstructure occurred through DRX due to decrease in deformation temperature and increase in the strain rate.

To the best of our knowledge, hardly any researchers studied critical phase regime control MAF in order to obtain better combination of mechanical properties of IF and microalloyed steels. Furthermore, bulk ultrafine grained materials manufactured through MAF techniques although exhibits excellent mechanical properties. But the deformation characteristics might be weakened due to the decrease in strain hardening rate [16]. Thus, examination of fracture toughness is vital prior to any design applications, as this would provide adequate information about the fracture activities and deformation features of such submicron size grain materials [17]. But, due to the limited sample dimension of the ultrafine grained (UFG) steels obtained through most of the SPD techniques, the fracture toughness testing is challenging; Therefore, limited data is available about the valid plane strain fracture toughness i.e.  $K_{IC}$  of the submicron size grained materials. Recently, some researchers [18-20] made an effort to estimate the fracture toughness values through single edge bend tests and they have found that there is significant effect on the enhancement of conditional fracture toughness through grain size refinement of nonferrous UFG materials developed through cryoforging/cryorolling techniques. Recently, the application of IF and microalloyed steels have been spread in several sectors, such as, line pipe, automotive, ship building and several structural applications. Thus, the materials should have high yield strength along with good fracture toughness to use these materials for better performance for those applications. Hence, aim of the present investigation is to design multiaxial forging schedules in order to achieve submicron sized grains ( $<1\mu\text{m}$ ) microalloyed and IF steels, which could offer superior mechanical property along with good fracture toughness values. In the current study, investigation of fracture toughness has been performed through calculating  $K_Q$  (conditional fracture toughness),  $K_{ee}$  (equivalent energy fracture toughness) and  $J$ -integral (crack initiation energy) values from single-edge bend test data of the ultrafine grained samples and these fracture toughness values have been correlated with other mechanical properties and corresponding microstructural features evolved. Furthermore, the accumulated dislocation densities, lattice strain and crystallite size of the multiaxially forged specimens have been estimated through X-ray diffraction line profile analysis to explain the different strengthening mechanisms involved. Moreover, the value of yield strength has been calculated theoretically using Taylor's equation and correlated with the experimentally obtained values. Accordingly, effect of strain hardening rate and strain hardening exponent on the deformation behavior has also been investigated, and

correlated with the yield strength and uniform elongation. A quantitative fractography analysis was also executed to relate the ductility of the corresponding specimens.

## 2. Materials and experimental procedure

The materials used for the present study are Ti+Nb stabilized low carbon (C) microalloyed (MA) and interstitial free (IF) steels. The MA steel was manufactured and supplied by Steel Authority of India Limited (SAIL) and the IF steel used was produced and supplied by TATA Steel, Jamshedpur, India. The chemical compositions (wt.%) of those steels were examined by optical emission spectroscopy analysis and the analyzed results are presented in Table 1.

Table 1: Chemical composition (wt. %) of the low C microalloyed and IF steels.

Elements (wt. %)	C	Si	Mn	Al	Ti	Nb	S	P	N	Fe
IF steel	0.0026	0.007	0.14	0.052	0.042	0.012	0.008	0.031	0.002	99.7
MA steel	0.11	0.344	1.44	0.01	0.028	0.044	0.003	0.016	0.01	97.92

Multiaxial forging (MAF) was conducted using a screw press forging machine (Birson Industries) at  $\sim A_{r1}$  phase region (at  $\sim 650^\circ\text{C}$  for both microalloyed and IF steel specimens). The specimens were initially homogenized at  $1200^\circ\text{C}$  for 1h inside the inert gas atmosphere control furnace and afterwards the samples were multiaxially forged (MAFed) at the desired temperature  $\sim 650^\circ\text{C}$  at normal atmosphere. After each pass, the specimens were kept inside the muffle furnace at selected deformation temperature and held for 2-3 minutes to attain that particular temperature. A mixture of acetone and graphite powder was used as a lubricant during the MAF for homogeneous deformation [18,19]. Actually, graphite is miscible in acetone. Hence, acetone is used to make homogeneous mixture, which could be uniformly applied on the sample. Here, the graphite powder acts as a lubricant and helps in performing homogeneous deformation at high temperatures. The rectangular samples were machined out from the annealed samples to obtain the required dimension of  $30\text{mm} \times 24.5\text{mm} \times 20\text{mm}$  through maintaining the ratio of 1.5:1.22:1.0. Several researchers [21,22] have reported the estimation of the equivalent strains using well established von Mises criteria during large strain deformation in a channel die. Although, Onaka [23] has claimed that Hencky logarithmic strain criterion is more appropriate than the von Mises criteria to calculate the equivalent strain during SPD process. Moreover, Shrivastava et al. [22] confirmed that the effective shear stress associated with other stresses could provide an adequate description of von Mises equivalent strains, whereas, the Hencky

logarithmic strains are invalid. Furthermore, Segal [24] studied the applicability of both the approaches (i.e., von Mises and Hencky) to find out the equivalent strains during SPD process, and finally concluded that von Mises criterion works in both, simple shear and pure shear cases; while the Hencky logarithmic strain criterion is correct only for pure shear. Hence, in the present study we have used von Mises criteria in the estimation of the equivalent strains. After each pass of forging, the height of the specimen decreases from 30 to 20mm, which corresponds to a true strain component,  $\varepsilon_x = -0.4$ . As in the present study, forging has been carried out in a channel die, which resemble to a plane strain condition, where  $\varepsilon_x = -\varepsilon_y$  and  $\varepsilon_z = 0$ . Hence, the equivalent strain ( $\varepsilon_{eq}$ ) can be estimated using von Mises criteria as follows [21,22].

$$\varepsilon_{eq} = \left[ \frac{2}{9} \{ (\varepsilon_x - \varepsilon_y)^2 + (\varepsilon_y - \varepsilon_z)^2 + (\varepsilon_z - \varepsilon_x)^2 \} + \frac{1}{3} (\gamma_{xy} + \gamma_{yz} + \gamma_{zx}) \right]^{0.5} \quad (1)$$

Where,  $\gamma_{xy}$ ,  $\gamma_{yz}$ ,  $\gamma_{zx}$ , represents the shear strain component. As there is no shear strain applied in the present study, thus the sum of  $\gamma_{xy}$ ,  $\gamma_{yz}$ ,  $\gamma_{zx} = 0$ . As per this equation, the equivalent strain is calculated to be 0.5 for each pressing in the channel die. In the MAF method, after each pass, the sample was rotated by  $90^\circ$  followed by application of same equivalent true strain of  $\sim 0.5$  to the longest side at each MAF pass (Fig. 1).

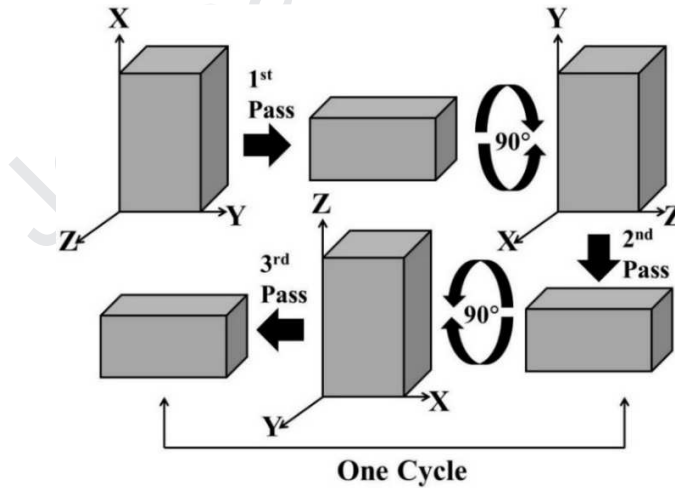


Fig. 1: Representation of multi-axial forging schedule for one cycle.

Fig. 1 represents the principle of MAF technique. True strain per pass is maintained a constant value for all the forging cycles and it is  $\Delta\varepsilon_i = 0.5$  (where 'i' number of forging passes). The cumulative true strain after 1 cycle of the forging is estimated to be  $\Sigma\Delta\varepsilon_{n=1} = (\Delta\varepsilon_1 + \Delta\varepsilon_2 + \Delta\varepsilon_3) = 1.5$  (where 'n' is number of forging cycles). The multi-axial forging was performed in a closed die at a strain rate of  $10s^{-1}$ . Forging die has been prepared using water hardened plain carbon tool



steels. The microalloyed steel samples were successfully forged up to 15 cycles (an equivalent total true strains of 22.5 i.e.  $0.5 \times 45$ ; 45 passes for 15 cycles), whereas, the IF steel samples were possible to forge up to 18 cycles (an equivalent total true strains of 27 ( $0.5 \times 54$ ; 54 passes for 18 cycles) without revealing any surface crack. In case of the microalloyed steel, when MAF was carried out beyond 15 cycles at  $650^\circ\text{C}$ , the both micro and macro-cracks were initiated at the surface. Similarly, in case of the IF steel specimens, initiation of crack were observed after 18 cycles MAF at  $650^\circ\text{C}$ . Thus, in the present study, the maximum forging cycles has been limited to 15 cycles in case of the microalloyed steel and to 18 cycles in case of the IF steel. In order to study the microstructural evolution and mechanical properties after MAF, the samples were sectioned along the highest dimension, i.e., from the plane perpendicular to the last forging axis. Samples for tensile test was performed using a universal testing machine (Tinius Olsen, S-Series, H25K-S) at a constant strain rate of  $2 \times 10^{-4} \text{ s}^{-1}$ . Specimens for tensile testing were prepared as per sub-size standard ASTM: E8. Fracture toughness of the homogenized annealed, 5cycles, 15/18cycles multiaxially forged microalloyed and IF steel samples were studied by conducting single edge bend tests at room temperature. The single edge bend tests were performed on same Tinius Olsen machine (25 kN capacity) with single edge bend test fixture, operated at a same strain rate ( $2 \times 10^{-4} \text{ s}^{-1}$ ). For single edge bend test, all the forged specimens have been machined as per the ASTM E399-05 standard, along the plane parallel to the forging direction (as represented in Fig. 2a and b). All the specimens for single edge bend test were fatigue pre-cracked through EDM wire cutting and maintained a crack length to the width ratio of 0.5 ( $a/W=3.75/7.5$ ). The thickness ( $B$ ) of 3-point bend sample is 3.75mm, while unbroken ligament  $b$  ( $W-a=b$ )=3.75mm maintained for all samples (Figs. 2a and b). The radius of the crack is 0.125mm. Three specimens in each conditions were tested and taken the average value for each type of specimens.

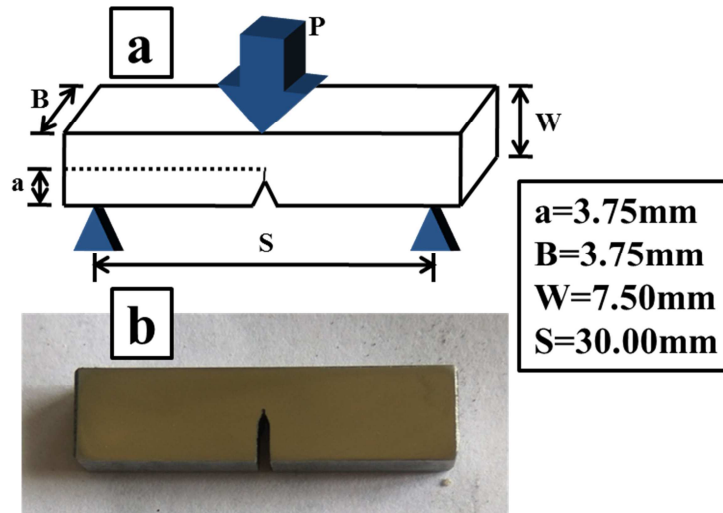


Fig. 2: (a) Schematic presentation of a single edge bend specimen, (b) micrograph of single edge bend specimen.

Microstructural investigation of multiaxially forged specimens was carried out through optical microscopy, scanning electron microscopy (SEM), transmission electron microscopy (TEM) and EBSD studies. In order to study optical microstructure (using Leica DMI5000M microscope), all the forged specimens were polished using different emery papers and cloth and subsequently etched by 2% Nital solution. In order to analyze high and low angle grain boundaries present and their distribution, EBSD analysis has been carried out. In this regard the selected specimens were initially polished using alumina powder followed by using colloidal silica. Finally, the specimens were electropolished for 50s using an electrolyte of 20% perchloric acid+80% methanol at  $-20^{\circ}\text{C}$  and 21V. EBSD detector was attached with SEM (ZEISS, 51-ADD0048). The step size and frame size was kept  $0.1\mu\text{m}$  and  $150\mu\text{m}\times 150\mu\text{m}$ , respectively. Analysis of EBSD image was carried out using HKL channel-5 system software. The surface which is parallel to the forging axis of the deformed specimen was analyzed. TEM study was performed using a transmission electron microscope (FEI Technai 20 G2S-Twin) operated at 200 kV. The specimens for TEM study were initially thinned down up to  $0.08\mu\text{m}$  by mechanical polishing. After that 3 mm disk specimens were punched out from the thin foil (using a Gatan disk cutter) followed by electro-polishing through a twin jet electro-polisher (FEI) using a solution of 10% perchloric acid+90% methanol at  $-20^{\circ}\text{C}$  using 40V. Analysis of fracture surfaces and mode of failure after single edge bend test were examined under SEM.

### 3. Results and discussion

#### 3.1 Microstructural characterization

Optical microstructure of the homogenized annealed (H-AN) microalloyed and IF steel samples are presented in Figs. 3a and b, respectively. Fig. 3a exhibits the presence of equiaxed pro-eutectoid ferrite along with lamellar pearlite with an average grain size of  $\sim 56\mu\text{m}$  whereas, Fig. 3b exhibits the presence of only equiaxed pro-eutectoid ferrite grains with an average grain size  $\sim 110\mu\text{m}$ . The existence of Pearlite is not identified in the microstructure of IF steel due to very low C content (0.0026%).

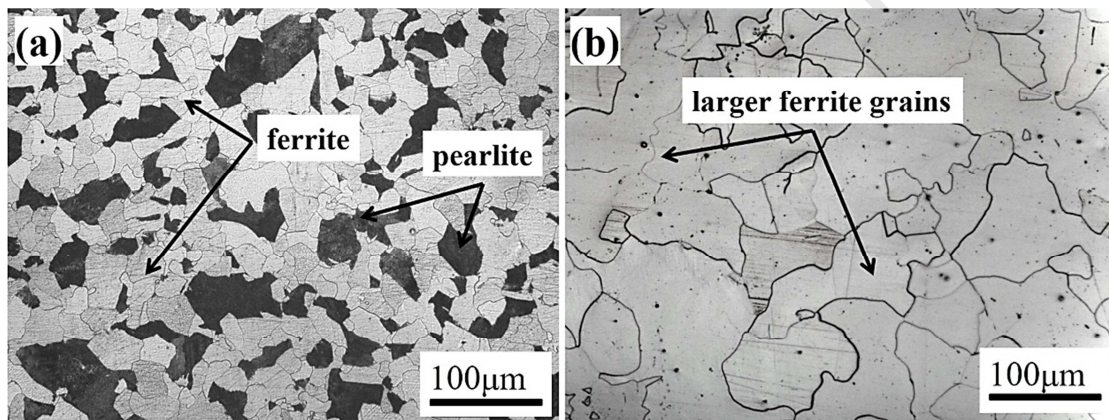


Fig. 3: Optical microstructure of homogenized annealed (a) microalloyed and (b) IF steel specimens.

Fig. 4a represents EBSD inverse pole figure map of  $\alpha+\gamma$  phase regime control 5 cycles MAFed microalloyed steel specimen. Fig. 4b represents the magnified image of the selected location as indicated using dotted line in Fig. 4a. Formation of ultrafine substructures (possibly  $<1\mu\text{m}$  size) along with fine ferrite grains of 2-3μm size can be seen from Fig. 4b. Moreover, EBSD grain boundary map along with grain average misorientation map of  $\alpha+\gamma$  phase regime control 5 cycles MAFed microalloyed steel specimen are also analyzed and presented in Fig. 4c. From Fig. 4c, it can clearly be noticed that new grains formed on the grain boundaries of the pre-existing grains. Furthermore, it can clearly be observed from the grain average misorientation map (Fig. 4c) that several low angle grain boundaries are introduced within the equiaxed ferrite grains, which clearly indicate that the original grains were subdivided through formation of low angle grain boundary by dynamic transformation. The ferrite grain boundaries demonstrated (Fig. 4b) that numerous low angle grain boundaries were introduced within the ferrite grains bounded by high angle boundaries. In addition, EBSD grain average misorientation map of the 5 cycles MAFed microalloyed steel specimen is also analyzed and represents in Fig. 4d.



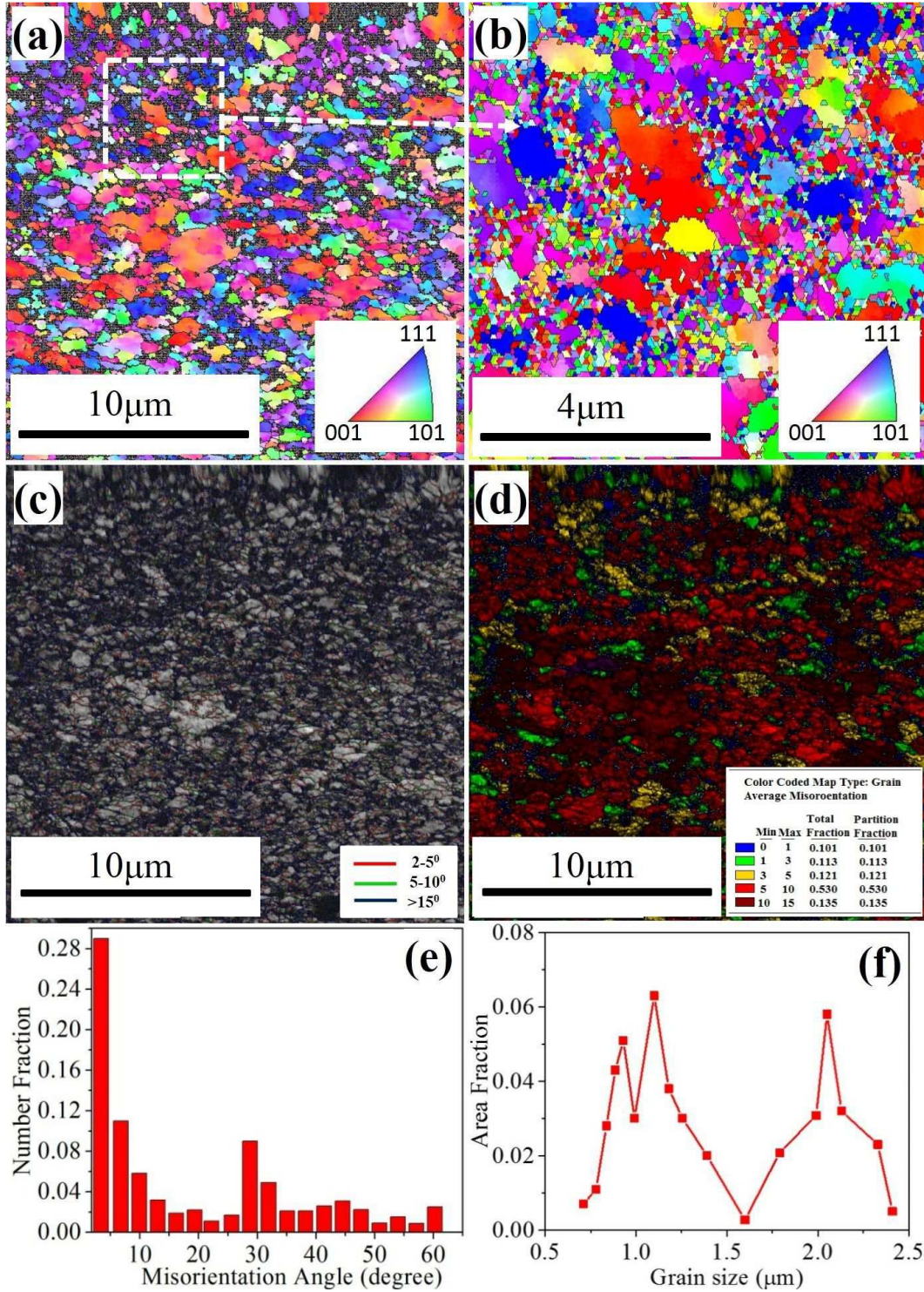


Fig. 4: (a) EBSD inverse pole figure map, (b) magnified image of the selected location as indicated using dotted line in Fig. 4a, (c) grain boundary map (d) grain average misorientation map of  $\alpha+\gamma$  region control 5 cycles MAFed microalloyed steel specimen, (e and f) misorientation profile and grain size distribution of corresponding specimen, respectively.

The grain average misorientation map exhibits a high fraction of deformed grains along with a small fraction of recrystallized grains. This is due to the fact that ferrite grain refinement in each pass during MAF is accomplished to the strain induced ferritic transformation of austenite grains, which showed a lower amount recrystallized grains.

Moreover, after 15 cycles of the MAF in this region, a uniformly distributed ultrafine ferritic subgrain structure was achieved (Figs. 5a,b). Figs. 5a and b represent the EBSD inverse pole figure image and grain boundary map of the 15 cycles MAFed microalloyed steel specimen. Uniform distribution of extremely fine ferrite grains are found to develop after 15 cycles of the MAF (Figs. 5a and b). Thorough examination of the misorientation profile, it can also be seen that the misorientation angle of the grain boundaries of the 15 cycles MAFed specimen (Fig. 5c) is comparatively higher than that of the 5 cycles MAFed sample (Fig. 4b). This is attributed to the extensive dynamic recovery of severely deformed ferrite grains and/or strain induced ferritic transformation during 15 cycles MAF at  $A_{r1}$  region. The average grain size is estimated to be ~280nm from the EBSD grain size distribution profile of the corresponding specimen. These sub-microstructural features are further analyzed in details through TEM analysis (discussed later).

During initial stages of deformation, the dislocation generates and starts accumulating within the material. The density of dislocation rises rapidly with further deformation, which initiates strain hardening within the dynamic recovery stage. This is competed by annihilation of dislocations as the dynamic restoration process is balanced by strain hardening. During this period, a microstructure of low angle boundaries subgrains develops. With further straining, the subgrain misorientations gradually increase until they attain high angle boundary (HAB) [8,9]. This type of process is referred to as dynamic recrystallization (DRX). In this process, the new grains form as a result of the increase in sub-boundary misorientation brought about by continuous accumulation of the dislocations introduced by the deformation [8,9].



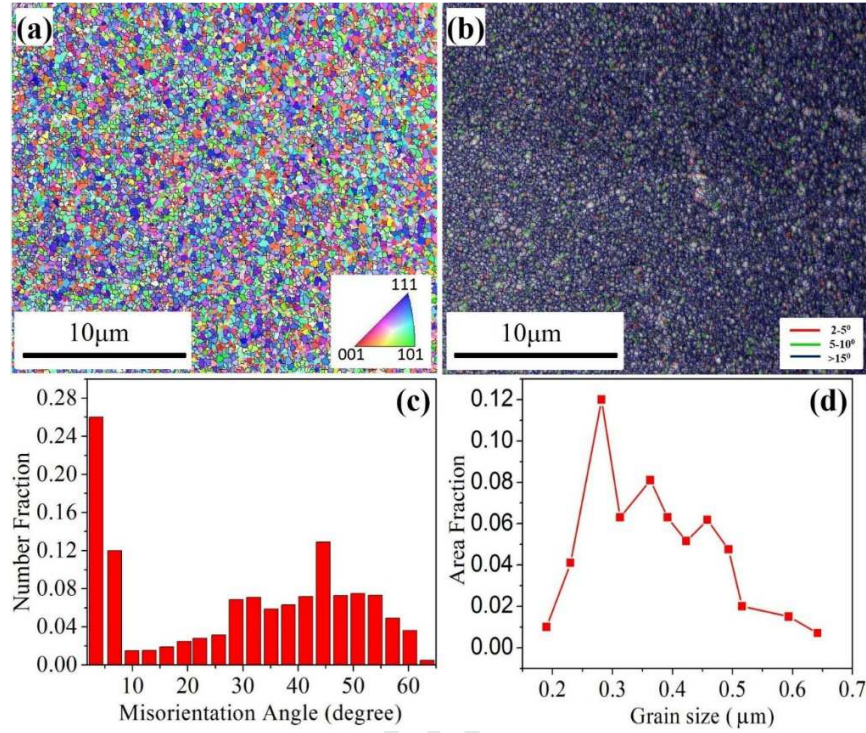


Fig. 5: (a) EBSD inverse pole figure map, (b) grain boundary map of 15 cycles MAFed microalloyed steel specimen, (c and d) misorientation profile and grain size distribution of corresponding specimen, respectively.

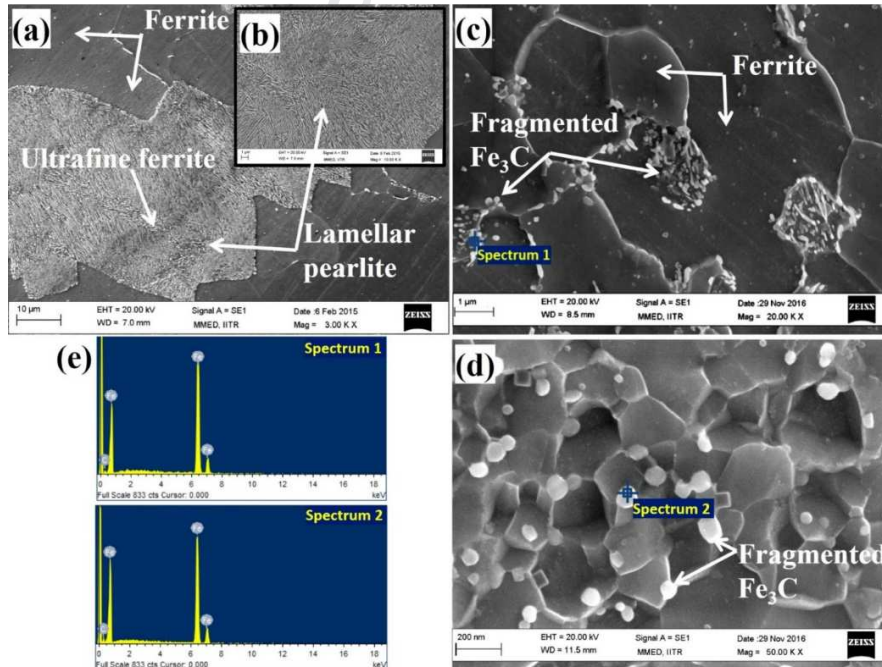


Fig. 6: SEM micrograph of (a) annealed, (b) magnified image Fig. 6a, (c) 5cycles and (d) 15cycles MAFed microalloyed steel (at  $\sim A_{r1}$ ) and (e) EDAX analysis on selected spot of the corresponding specimens.

Furthermore, it can also be noticed from the SEM micrographs that the starting material (annealed specimen) contains alternate plates of ferrite and cementite ( $\text{Fe}_3\text{C}$ ), i.e. lamellar pearlite (Figs. 6a,b). With increasing the number of MAF cycles, interesting deformation features could be observed in the pearlite colonies as shown in SEM images in Figs. 6c and d. A small fraction (15-20%) of distorted lamellar pearlite structure can be seen in Fig. 6c after 5 cycles of MAF at  $650^\circ\text{C}$ . This indicates the beginning of fragmentation and refining of cementite ( $\text{Fe}_3\text{C}$ ) in the pearlite colonies after 5 cycles. Moreover, after 15 cycles MAF, exciting deformation features could be seen in the pearlite colonies as shown in SEM image in Fig. 6d. Extensive fragmentation of  $\text{Fe}_3\text{C}$  phase into nanometer level particles ( $\sim 35\text{nm}$  size particles) could be observed after 15 cycles of MAF at  $650^\circ\text{C}$  (Fig. 6e). It can also be noticed from Fig. 6c that the  $\text{Fe}_3\text{C}$  particles were not only fragmented (avg. fraction is  $\sim 12\text{-}15\%$ ) but also distributed homogeneously within the ferrite matrix after 15 cycles of MAF at  $650^\circ\text{C}$ . The EDAX point analysis confirms the existence of  $\text{Fe}_3\text{C}$  particles through revealing the strong peaks of Fe and C as shown in Fig. 6e.

Thus, the maximum grain refinement was achieved when the microalloyed steel specimen MAFed up to 15 cycles in the  $\alpha+\gamma$  region at  $650^\circ\text{C}$  (at  $\sim A_{r1}$ ). Due to continuous application of high strain in repeated direction the coarser ferrite grains get strain hardened through continuous buildup of large strain which yield the creation of high density dislocation substructures, both at the ferrite boundaries and inside the grains. These substructures finally form a fine grained ferrite [25-27] through strain induced ferritic transformation to form ultrafine structures, which are finally recovered to generate new equiaxed ferrite grains. Also, during multidirectional deformation, the pearlitic structure is fragmented into ultrafine size and distributed uniformly along with the ultrafine ferritic grains. It is now well recognized that the ferrite grain size can effectively decrease through strain induced ferrite transformation (SIFT) and this process is favorable at relatively lower deformation temperature [28]. During MAF in 3 different directions, microshear bands can form in various directions direction which endorses dislocations activation, accumulation and rearrangement between them followed by alteration of the low angle grain boundaries to high angle boundaries and thereby increase in the grain boundaries misorientation and finally leads to the development of ultrafine ferrite grains [29].

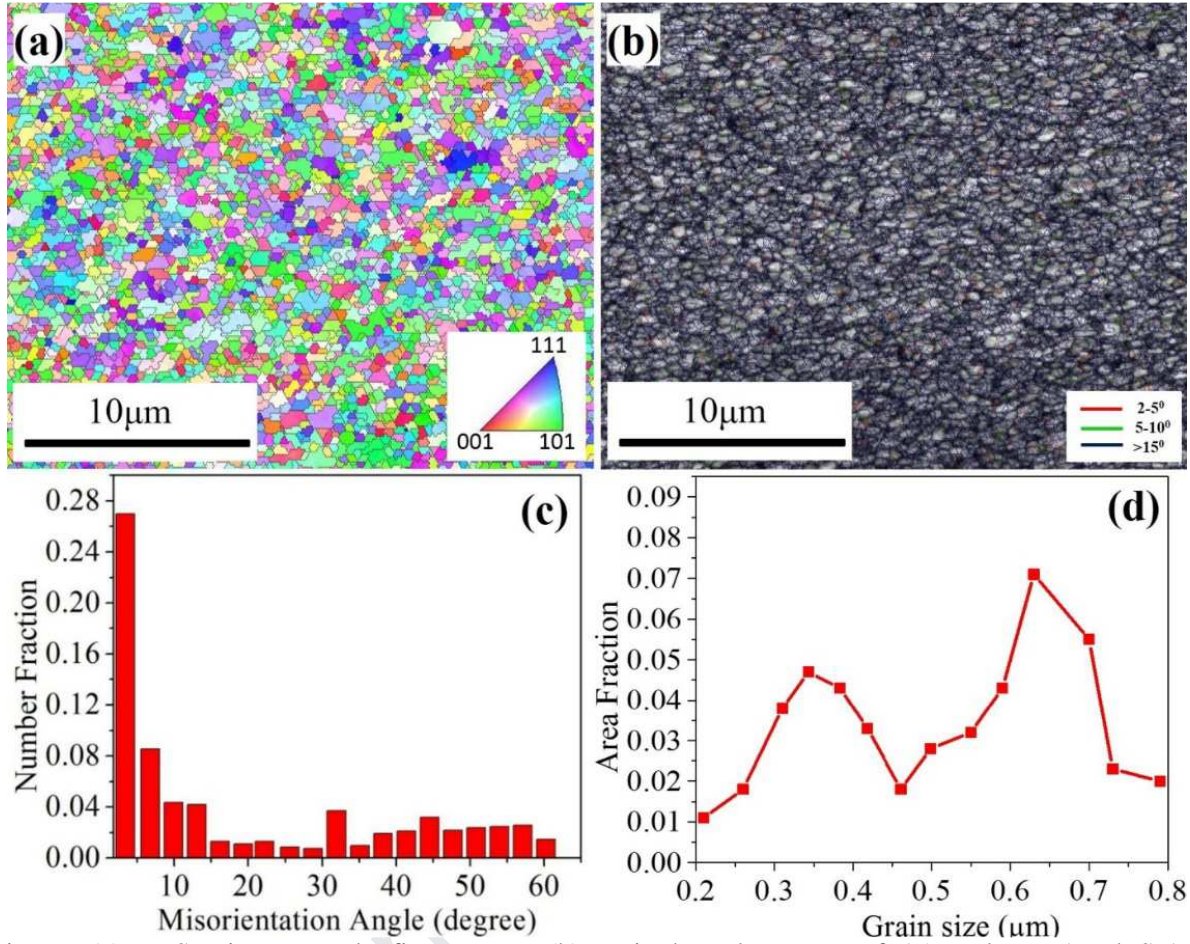


Fig. 7: (a) EBSD inverse pole figure map, (b) grain boundary map of 15 cycles MAFed+S-AN microalloyed steel specimen, (c and d) misorientation profile and grain size distribution of corresponding specimen, respectively.

Furthermore, after multiaxial forging at  $\sim A_{r1}$  region, the 15 cycles forged specimen was short-time annealed at 700°C for 180s in order to improve the ductility of the steel. Grain recrystallization and growth are greatly affect with the annealing time and temperature [30]. Hence, in the present study, optimum annealing time of 180s at 700°C was selected to avoid the deterioration of mechanical properties. Figs. 7a and b signifies the EBSD inverse pole figure image and grain boundary map of the MAFed (15cycles)+short-annealed (S-AN) microalloyed steel specimen. Bimodal distribution of ferrite grains are found to develop after short-annealing treatment (Fig. 7a and b). The grain size distribution of the corresponding specimen was carried out through EBSD analysis (Fig. 7d) for better clarity of the microstructure. A bimodal grain size distribution consisting of relatively larger size ( $\sim 660$ nm) and finer size (340nm) grains could clearly be observed from the EBSD image (Fig. 7d) of the MAFed+S-AN sample. This is



attributed to the partial recrystallization and recovery of the heavily deformed structure during the S-AN treatment.

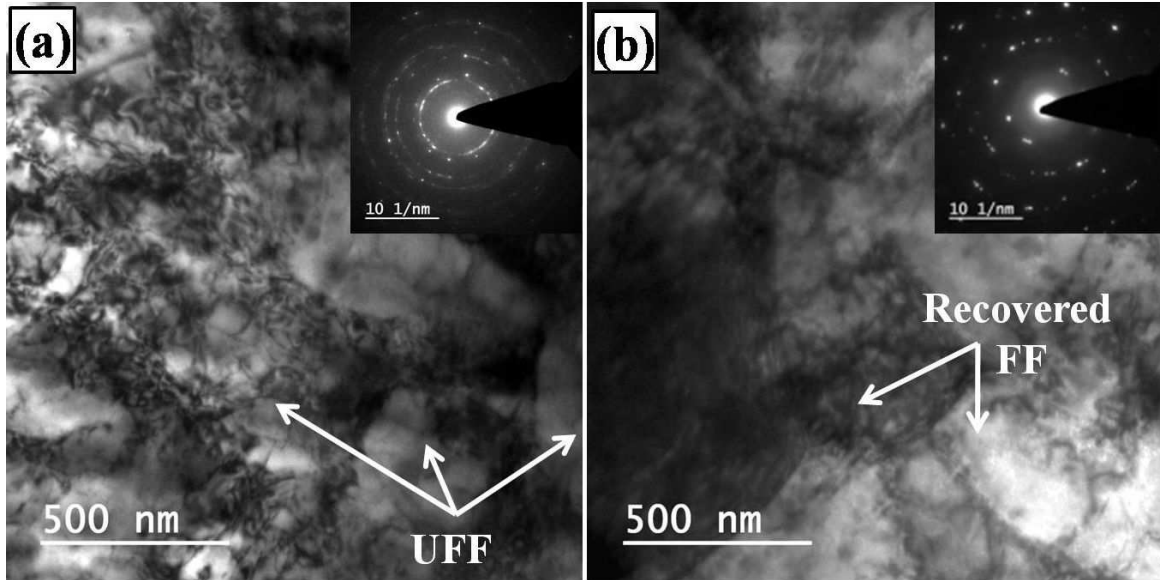


Fig. 8: TEM bright field image of microalloyed steel specimens: (a) MAFed (15 cycles) at  $\sim A_{r1}$  region and (b) MAFed (15 cycles)+S-AN.

TEM bright field micrographs of the 15 cycles MAFed (at  $A_{r1}$  region) and MAFed+S-AN specimens are shown in Figs. 8a and b, respectively. The corresponding selected area electron diffraction pattern (SAED) is shown in the inset of Figs. 8a and b. Fig. 8a shows the presence of high fraction of ferrite substructures (avg. size 280nm) with high density of dislocations. The associated SAED shows circular ring like pattern which substantiates the existence of nanosize grains. On the other hand, a bimodal distribution of equiaxed ultrafine ferrite structure consisting of relatively larger size ( $\sim 660$ nm) and finer size (340nm) grains could be observed from Fig. 8b. The associated SAED pattern shows spotty rings which substantiate the existence of relatively larger size grains as compared to that of the MAFed specimen without annealing. The partial recrystallization and dislocation annihilation during S-AN treatment could allow to grow the grains a bit.

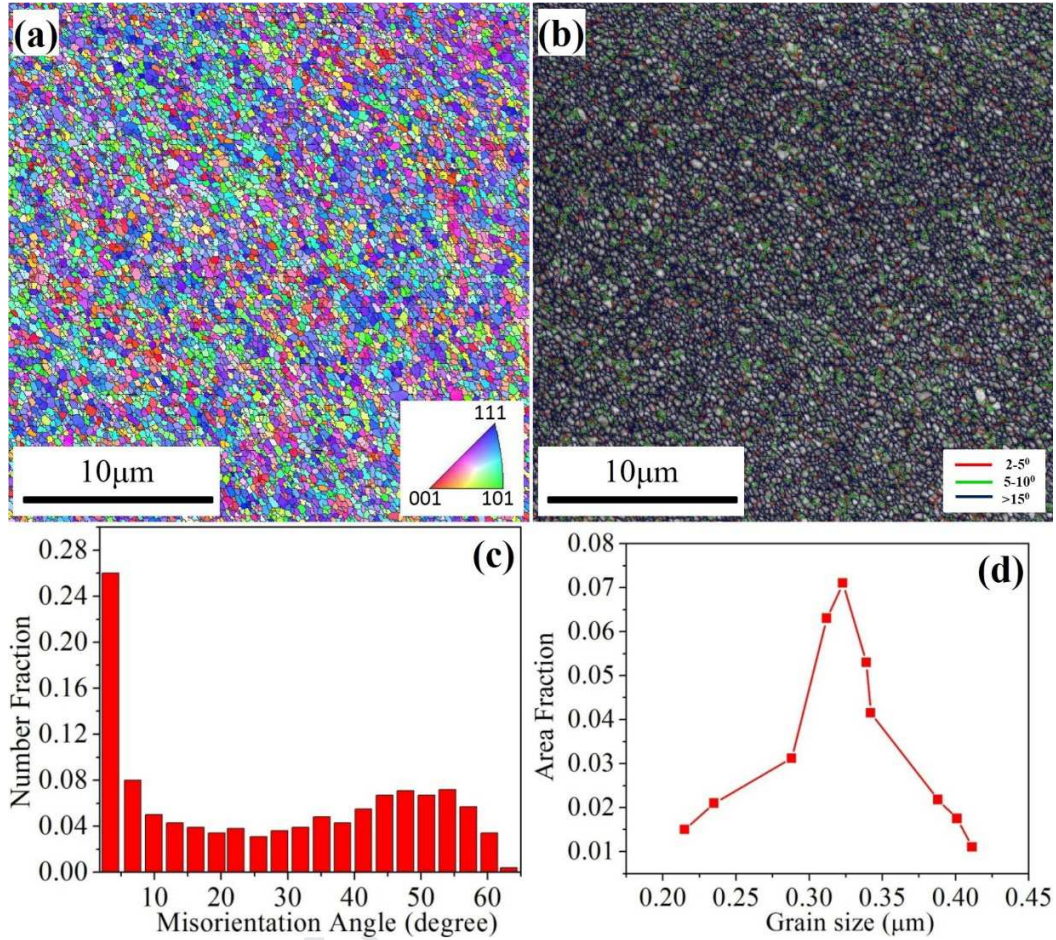


Fig. 9: (a,c) EBSD inverse pole figure map, (b,d) grain boundary map of 18cycles MAFed and MAFed+S-AN IF steel specimens, respectively, (c and d) misorientation profile and grain size distribution of corresponding specimen, respectively.

Similarly, in the case of IF steel, a uniformly distributed ultrafine ferritic grain structure with an avg. grain size of  $\sim 320\text{nm}$  is achieved (Figs. 9a and d) after 18 cycles of MAF through strain induced ferritic transformation and recovery of heavily deformed ferrite grains. In this case also after multiaxial forging at  $\sim A_{r1}$  region, the 18 cycles forged specimen was short-time annealed at  $850^\circ\text{C}$  for 100s in order to improve the ductility and formability of the steel. The grain size distribution of the MAFed (18 cycles)+short-annealed (S-AN) sample was carried out through EBSD analysis (Fig. 10 a and d). A bimodal grain size distribution consisting of relatively larger size ( $\sim 535\text{nm}$ ) and finer size ( $330\text{nm}$ ) grains could clearly be observed (Fig. 10d) from the EBSD grain size distribution profile of the MAFed+S-AN sample.



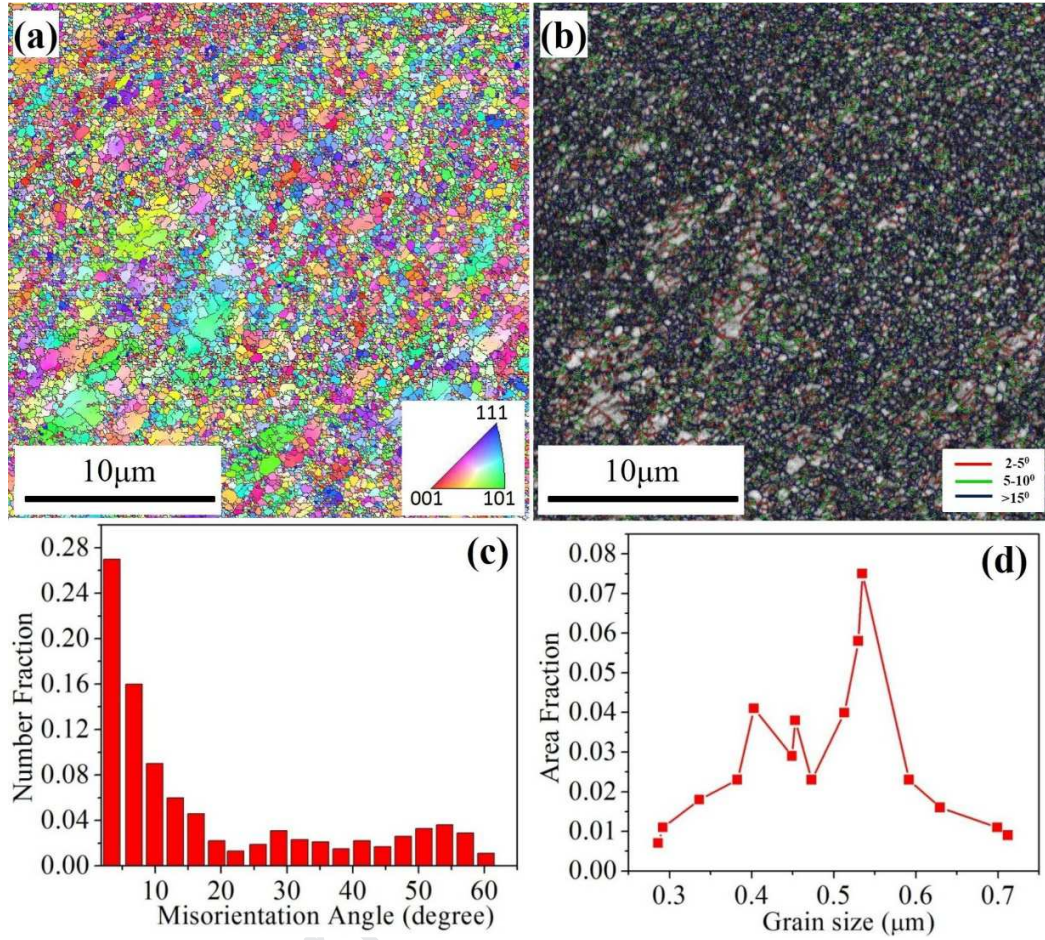


Fig. 10: (a,c) EBSD inverse pole figure map, (b,d) grain boundary map of 18cycles MAFed and MAFed+S-AN IF steel specimens, respectively, (c and d) misorientation profile and grain size distribution of corresponding specimen, respectively.

TEM bright field micrographs of the 18 cycles MAFed (at  $A_{r1}$  region) and MAFed+S-AN specimens are shown in Figs. 11a and b, respectively. The corresponding selected area electron diffraction pattern (SAED) is shown in the inset of Figs. 11a and b. Fig. 11a shows the presence of high fraction of ferritic substructure (avg. size 320nm) with high density of dislocations. The associated SAED shows circular ring like pattern which substantiates the existence of submicron size grains. On the other hand, a bimodal distribution of equiaxed ultrafine ferrite structure consisting of relatively larger size (~535nm) and finer size (345nm) grains could be observed from Fig. 11b. Also, the bimodal grains contain relatively less amount of dislocation density. The associated SAED pattern shows spotty rings which substantiate the existence of relatively larger size grains as compared to that of the MAFed specimen without annealing. The partial recrystallization and dislocation annihilation during S-AN treatment could allow to grow the

grains up to a certain level. The mechanism of formation of the ultrafine ferrites, could be described in the same way, as explained above for the microalloyed steel samples.

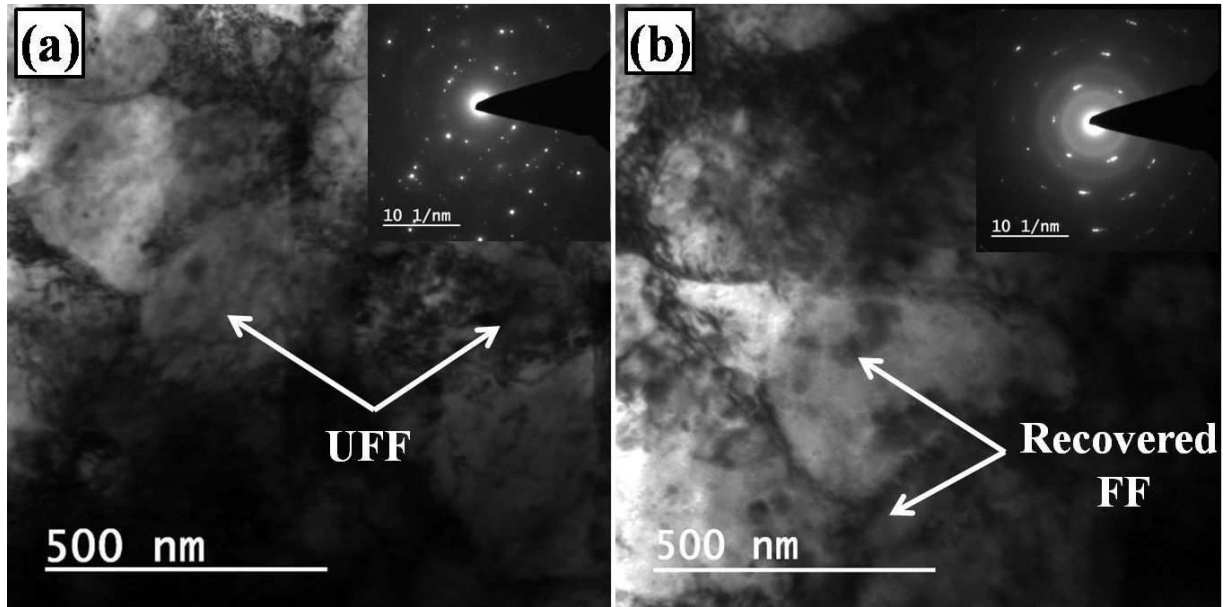


Fig. 11: TEM bright field image of IF steel specimens: (a) MAFed for 18 cycles at  $\alpha$  region and (b) MAFed (18 cycles)+S-AN.

### 3.2 Mechanical Properties

The engineering stress-strain curves of the homogenized anneal and MAFed specimens are shown in Figs. 12a,b and summarized in Table 2. The YS of the homogenized anneal microalloyed and IF steel samples is found to be 251 and 141MPa with a % elongation 33 and 46%, respectively. The high amount of % elongation is attributed to the presence of large size equiaxed ferrite and lamellar pearlite (avg. grain size of  $\sim 56\mu\text{m}$ ) in case of microalloyed steel and comparatively larger size ferrite grains (avg. grain size of  $\sim 110\mu\text{m}$ ) in case of IF steel specimens.

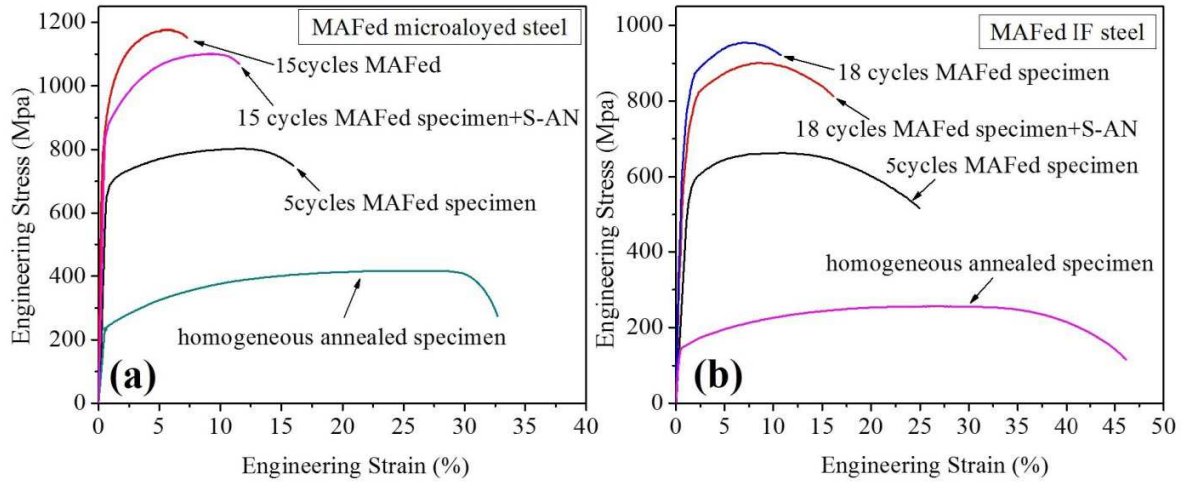


Fig. 12: Tensile stress vs. strain plots of MAFed (a) microalloyed and (b) IF steel specimens.

Table 2: The Mechanical properties of the Homogenized annealed (H-AN) and MAFed microalloyed and IF steel specimens.

Forging conditions		YS (MPa)	UTS (MPa)	%Elongation
Microalloyed steel	H-AN sample	251±4	440±5	33±1.7
	5 cycles MAFed at 650°C	811±8	937±9	19±1
	15 cycles MAFed at 650°C	1027±6	1171±8	8.3±1.5
	15 cycles MAFed at 650°C+S-AN	949±4	1097±3	12.60±1.5
IF steel	H-AN sample	141±3	256±5	46±1.7
	5 cycles MAFed at 650°C	601±6	627±8	25.2±1
	18 cycles MAFed at 650°C	881±5	978±3	11.2±2
	18 cycles MAFed at 650°C+S-AN	817±6	849±4	15.6±1

The YS (Fig. 12a) of the 5 cycles MAFed microalloyed steel specimen deformed at  $\sim Ar_1$  region is found to increase to a high value (811MPa) than that of the homogenized specimen (YS=251 MPa). Moreover, after 15 cycles MAFed at the same region, the corresponding YS (1027MPa) improved more than 4 times than that of the starting material (251MPa). Furthermore it can also be observed that ductility of the 5cycles MAFed specimen decreased to  $\sim 19\%$ , which corresponds to ultrafine substructures ( $<1\mu m$  size) along with fine ferrite grains of 2-3 $\mu m$  size (Fig. 4a,b). Moreover, the microalloyed steel specimen after 15 cycles MAFed at  $\sim Ar_1$  region showed a total elongation of  $\sim 8.3\%$ . Earlier, it is already demonstrated that the microstructure of the corresponding specimen deformed at the pure ferritic region is consist of uniformly distributed ultrafine grain (280nm) ferrite along with nanosize (35nm) fragmented  $Fe_3C$  particles.

Therefore, it can be seen that the YS of the MAFed specimen is considerably improved with expense of their ductility, when forged in the ( $\sim Ar_1$  region) ferritic phase regime. Furthermore, it was found that the short annealing treatment after 15 cycles MAF significantly improved the ductility (12.5%) without much altering their YS (949MPa). This is mainly due to the partial recrystallization and recovery of ferrite grains during S-AN treatment and developed a bimodal grain structure. Thus, the bimodal grain size distribution could be obtained by MAF+S-AN treatment, which recover a certain amount of ductility without much sacrificing its strength. Bodin et al. [31] also reported the improvement of the YS without much sacrifice of ductility due to the formation of dual size grain distribution of ferrite grains in C-Mn steel after dual phase rolling within intercritical region i.e 825-775°C.

Similarly, the IF steel specimen MAFed in  $\alpha$  ferritic region (18 cycles) show the extreme improvement of the YS, and the corresponding value is 881MPa (Fig. 12b). It can be seen that the improved YS (881MPa) is more than 6 times higher as compared to the starting material (141MPa). Moreover, from Fig. 12b, it can also be observed that the specimen MAFed in  $\alpha$  ferritic region exhibited a total elongation of 11.2%. This is attributed due to the formation of uniformly distributed submicron size ferrite grains (320nm). Verma et al. and Cizek et al. [5,32] also reported the enhancement of mechanical properties of IF steel through grain size refinement by performing high pressure torsion at room temperature. They have demonstrated that grain size refinement along with dislocation strengthening is the key to enhancement of the YS. Furthermore, in the present investigation, it was also found that the short annealing treatment after 18 cycles MAF significantly improved the ductility (15.6%) without much altering its YS (817MPa). This is ascribed to the partial recrystallization and recovery of ferrite grains during S-AN treatment and developed a bimodal grain structure. Thus, the bimodal grain size distribution could be obtained by MAF+S-AN treatment, which can recover a certain amount of ductility without much sacrificing its strength. Effectiveness of short annealing treatment has also been investigated by several researchers [5,7]. Overall, it is also to be noted that the enhancement of the YS of the MAFed samples corroborated well with the hardness values of the corresponding samples.



### 3.3 Analysis of strengthening mechanisms

In order to study the effect strengthening due to strain hardening, the dislocation density of the multi-axially forged specimens (both microalloyed and IF steels) was estimated through X-ray diffraction (XRD) analysis. The XRD patterns of the forged microalloyed and IF specimens processed at different conditions are shown, respectively, in Figs. 13a and b. Width of the peaks of both the steel specimens is found to be broadened with increasing the number of forging cycles (Figs. 13a,b). This is attributed to the increase in the dislocation lattice strain and the refinement of the crystallite size [33]. Lattice microstrain and crystallite size have been calculated as per Williamson-Hall technique through the analysis of average peak broadening of 3 peaks of each specimen using the plot between  $B_r \cos \theta$  vs.  $\sin \theta$  [34]. Standard broadening data of polycrystalline  $Al_2O_3$  has been used to exclude the instrumental peak broadening from the total broadening as follows [34]:

$$\beta_r = \sqrt{\beta_{obs}^2 - \beta_i^2} \quad (2)$$

Where,  $\beta_r$  is the total broadening due to the lattice microstrain and crystallite size.  $\beta_i$  and  $\beta_{obs}$  are the integral breadth at the full width at half intensity maxima (FWHM) of the standard  $Al_2O_3$  and multi-axially forged specimens, respectively.

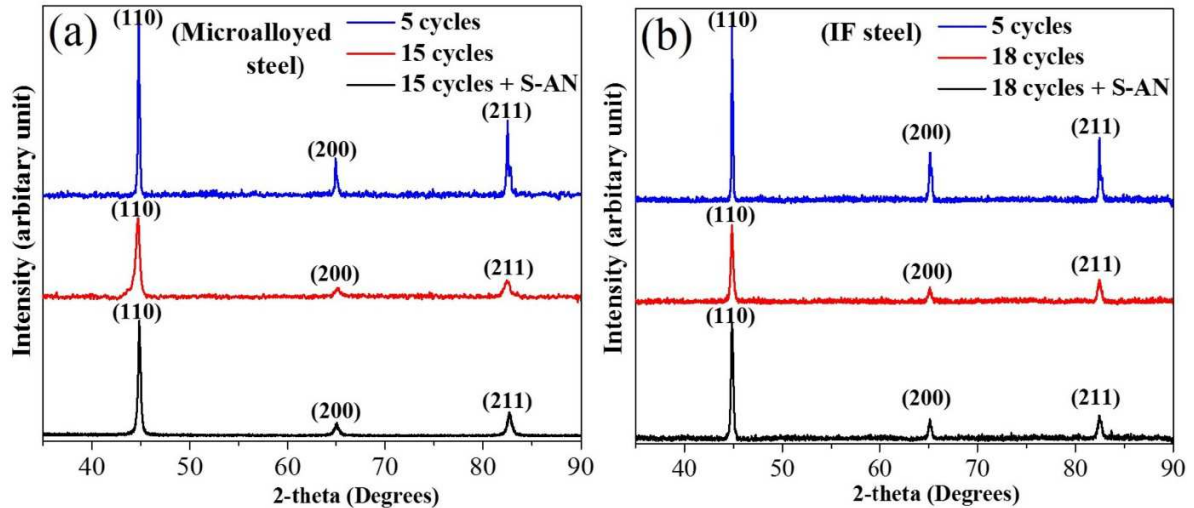


Fig. 13: X-ray diffraction pattern of the (a) MAFed microalloyed and (b) IF steels specimens at different processing conditions.

Finally, the density of dislocation ( $\rho_d$ ) can be calculated from Eq. 3 [36] through inserting the value of the lattice microstrain ( $\epsilon$ ) and average crystallite size ( $D$ ):

$$\rho_d = \frac{2\sqrt{3}(\epsilon^2)^{\frac{1}{2}}}{Db} \quad (3)$$

where,  $b$  is the Burgers vector. For BCC ferrite,  $b = a\sqrt{3}/2$ , where  $a = 0.28664$  nm [35]. The calculated values of lattice microstrain, crystallite size and dislocation density of the multiaxially forged IF and microalloyed steel specimens are tabulated in Tables 3 and 4.

Table 3: Lattice microstrain, crystallite size and amount of dislocation density, predicted and experimentally obtained YS for MAFed IF steel at different conditions.

Processing schedules	Crystallite size (nm)	Lattice microstrain ( $\times 10^{-3}$ )	Dislocation ( $m^{-2}$ )	$\sigma_{Taylor}$ (MPa)	$\sigma_y$ (MPa)
MAF 5 cycles	46.22	4.33	$1.31 \times 10^{15}$	765	$601 \pm 6$
MAF 18 cycles	29.59	5.57	$3.90 \times 10^{15}$	1072	$881 \pm 5$
MAF 18 cycles+S-AN	35.57	5.05	$2.22 \times 10^{15}$	985	$817 \pm 6$

Table 4: Lattice microstrain, crystallite size and amount of dislocation density, predicted and experimentally obtained YS for MAFed microalloyed steel at different conditions.

Processing schedules	Crystallite size (nm)	Lattice microstrain ( $\times 10^{-3}$ )	Dislocation ( $m^{-2}$ )	$\sigma_{Taylor}$ (MPa)	$\sigma_y$ (MPa)
MAF 5 cycles	39.57	5.17	$2.03 \times 10^{15}$	945	$811 \pm 8$
MAF 15 cycles	22.43	6.21	$6.53 \times 10^{15}$	1293	$1027 \pm 6$
MAF 15 cycles+S-AN	29.65	5.58	$3.29 \times 10^{15}$	1071	$949 \pm 4$

It can be seen that the average lattice microstrain raised from  $1.31 \times 10^{15}$  and  $2.03 \times 10^{15}$ , respectively, for the 5 cycles forged IF and microalloyed steel specimens to  $3.90 \times 10^{15}$  and  $6.53 \times 10^{15}$  corresponding to the 18 and 15 cycles forged (IF and microalloyed steel) specimens. Using the same technique, Sarkar et al. [37] evaluated the dislocation density of equal channel angular processed IF steel at a strain of 1.15 and 4.6, and reported the corresponding values  $3.6 \times 10^{14} m^{-2}$  and  $6.88 \times 10^{14} m^{-2}$ , respectively. In the current study, the values of dislocation density obtained for the multiaxially forged IF and microalloyed steel specimens are found quite higher as the forging was carried out at large equivalent strain (i.e. 22.5 and 27, respectively, for 15 and 18 cycles MAFed microalloyed and IF steel specimens). Accumulation of large amount of lattice strain yields the formation of high density dislocation substructures within the ferrite grains [38]. Furthermore, in case of the short annealed specimens after 15 and 18 cycles forging, the dislocation density found to decrease to  $3.29 \times 10^{15}$  and  $2.22 \times 10^{15}$ , respectively. This is accomplished to the partial recovery of highly dense substructures during very short time annealing.



Furthermore, the value of yield strength also has been estimated using Taylor's equation [35] and tabulated in Tables 3 and 4;

$$\sigma_{Taylor} = \sigma_0 + \alpha M G b \langle \rho \rangle^{1/2} \quad (5)$$

where,  $G$  is the shear modulus (value is 82 GPa),  $\sigma_0$  is the friction stress (value is 30 MPa),  $\alpha$  is a constant ( $\alpha$  is taken as 0.33),  $M$  is the Taylor factor (value is 3 for un-textured polycrystalline materials) and  $b$  is the Burgers vector (value is 0.25 nm) [37]. It can be observed that theoretically estimated yield strength (Tables 3 and 4) using Taylor's equation is higher than the experimentally obtained YS for both microalloyed and IF steel specimens. It can be remembered that for the theoretical calculations, the material is always assumed to be isotropic with respect to all strengthening mechanisms. But practically, always some defects are exist within the material and it is anisotropic in nature in that sense. Hence, the practically obtained yield strength value always be lower than that of the theoretically calculated value. Therefore, it can be concluded that the theoretical yield strength of the present material correlates well with the experimentally obtained values.

### 3.4 Strain hardening behavior

It is well-known that the strain hardening rate ( $\theta$ ) and strain-hardening exponent ( $n$ ) are two basic parameters, which mainly determines the flow behavior of a material when it is deformed [35]. In the present study, smooth true stress-true strain curves were employed to derivate the strain hardening rate, ( $\theta = \partial\sigma / \partial\epsilon$ ). This calculated data then has been plotted as a function of true stress. On the other hand, strain hardening exponent ( $n$ ) has been calculated from the slope of the logarithmic plot of the equation  $\sigma = K\epsilon^n$  ( $\log \sigma = \log K + n \log \epsilon$ ) [35].

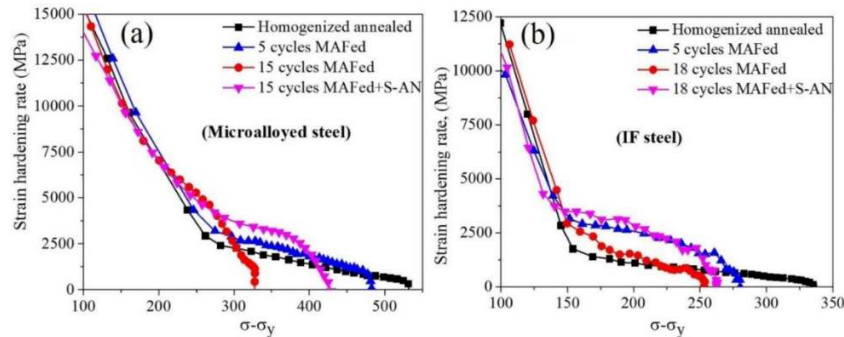


Fig. 14: (a,b) strain hardening rate vs. true stress curves of multiaxially forged microalloyed and IF steels at different processing conditions.

Figs. 14a,b represent the work hardening rate as a function of true stress of multiaxially forged microalloyed and IF steels at different processing conditions. It is observed that both multiaxially forged microalloyed and IF steels specimens showed a slower work hardening rate reduction than that of the annealed specimens. It is also found that the work hardening rate of the forged specimen gradually decreased with increasing the number of forging cycles. This is attributed to the fact that with increasing the amount of strain, materials gets strain harden as compared to the annealed condition. Furthermore, the multiaxial forging at large equivalent strain could generate high amount of dislocation substructure within the ferrite grains and thereby would hinder the dislocation movement [37]. Moreover, the short annealing treatment after multiaxial forging showed noticeable improvement in the strain hardening capacity when compared to as-forged counterpart. This is attributed to the partial recovery of the deformed grain structure, which could provide more scope for further deformation under static loading.

Furthermore, Figs. 15a,b represents the variation of uniform elongation and yield strength as a function of the strain hardening exponent ( $n$ ), respectively, for the multiaxially forged microalloyed and IF steel specimens as compared to that of the homogenized annealed counterparts.

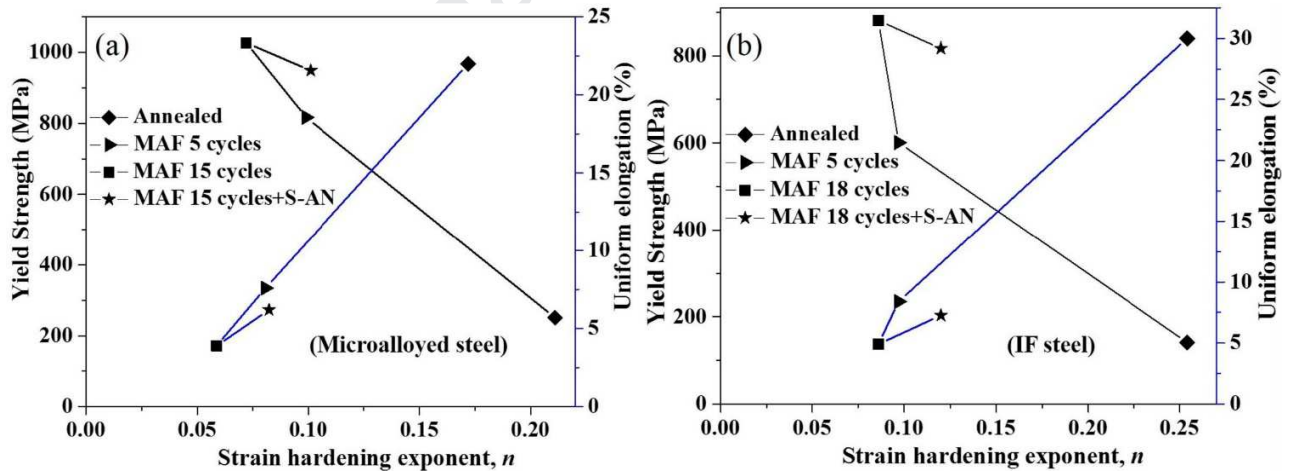


Fig. 15: Variation of Uniform elongation (UE) and yield strength (YS) and with strain hardening exponent ( $n$ ).

In case of the annealed specimen, the value of  $n$  is calculated to be 0.221 and 0.254, respectively, for microalloyed and IF steels. After multiaxial forging, the value of  $n$  is found to decrease steadily with enhancement of the yield strength. The minimum value of  $n$  reaches to 0.072 and 0.086 corresponding to the yield strength of 1027 and 601 MPa, respectively, for 15 cycles forged

microalloyed and 18 cycles forged IF steel specimens. Consequently, the uniform elongation is found to be more for the sample having high value of  $n$ . It can be observed from Figs. 15a,b that the annealed specimens, which showed a large uniform elongation (i.e., 22 and 30%) have the highest values of  $n$  (i.e. 0.211 and 0.254). The materials having large uniform elongation and low yield strength are usually associated with large work-hardening capacity. Hence, uniform elongation inversely related with the yield strength [39]. It can clearly be observed (Figs. 15a,b) that the maximum yield strength of 15 cycles forged microalloyed and 18 cycles forged IF steels are 1027 and 601 MPa, , respectively, with corresponding uniform elongation of only ~3.7 ( $n=0.072$ ) and 4.9% ( $n=0.086$ ). On the other hand the maximum value of uniform elongation reaches to ~22 ( $n=0.211$ ) and 30% ( $n=0.254$ ) corresponding to the yield strength of 251 and 141MPa for the annealed samples of both microalloyed and IF steels. It was observed that the extent of work hardening generally is very less in the severely deformed (e.g. MAF-processed) materials. This can be attributed to the increase in strain rate sensitivity with strain [1,3]. Moreover, it could be observed that the short annealed treatment after forging, there is an increase in the uniform elongation (7.4 and 6.2%, respectively, for microalloyed and IF steels) and strain hardening exponent (0.101 and 0.12, respectively, for microalloyed and IF steels) without losing much of the strength. This is ascribed to the partial recovery of the deformed grain structure, which could provide more scope for further deformation under static loading.

### 3.3 Fracture toughness analysis of submicron sized grained steels

Investigation of fracture toughness provides more insight about the deformation characteristics of submicron sized grain materials [17]. But, due to the limited sample geometry of the ultrafine grain steels obtained through most of the SPD techniques, the fracture toughness testing is challenging; Therefore, limited data is available about the valid plane strain fracture toughness i.e.  $K_{IC}$  of the ultrafine grained materials. Recently, some researchers [18-20] made an effort to estimate the fracture toughness values through single edge bend tests and they have found that there is significant effect on the enhancement of conditional fracture toughness through grain size refinement of nonferrous UFG materials developed through cryoforging/cryorolling techniques. Hence, in the present study, fracture toughness analysis of MAFed microalloyed and IF steel samples has been carried out through computing conditional fracture toughness ( $K_Q$ ), equivalent energy fracture toughness ( $K_{ec}$ ) and  $J$ -integral (crack initiation energy) from single

edge bend test data and correlated with other mechanical properties. The single edge bend test samples were prepared according to the ASTM E399-05 standard. Figs. 16b and c represent load vs. displacement curve of the MAFed microalloyed and IF steels specimens at different conditions. The value of apparent fracture toughness could be estimated from Eq. 6 as follows:

$$K_Q = \frac{P_Q}{B} \frac{s}{W^{3/2}} \left[ 2.9 \left( \frac{a}{W} \right)^{\frac{1}{2}} - 4.6 \left( \frac{a}{W} \right)^{\frac{3}{2}} + 21.8 \left( \frac{a}{W} \right)^{\frac{5}{2}} - 37.6 \left( \frac{a}{W} \right)^{\frac{7}{2}} + 38.7 \left( \frac{a}{W} \right)^{\frac{9}{2}} \right] \quad (6)$$

where,  $P_Q$  represent the maximum recorded load (at which pre-existing crack grows to a critical size and then comes out) and  $a$  is the length of the crack. Estimation of the value of  $P_Q$  from the load vs. extension curve of selected specimen is shown Fig. 16a. Furthermore, we can verify the applicability of the test, as per minimum thickness requirement for valid  $K_{IC}$  calculation under plane strain conditions through using the Eq. 7 as follows [40]:

$$B = 2.5 \left( K_Q / Y_S \right)^2 \quad (7)$$

In this case,  $K_Q$  can be accepted as plain strain fracture toughness ( $K_{IC}$ ), if the value of  $B$  is less than both the thickness as well as crack length of the sample [40]. Otherwise  $K_Q$  is considered as conditional fracture toughness.

It can be seen from the Fig. 16a that the value of  $P_Q$  is  $\sim 2654N$  for the 5 cycle MAFed IF steel sample. Hence, the value of  $K_Q$  is estimated to be  $69.7MPa\sqrt{m}$  for the 5 cycles MAFed IF steel sample through placing the values of  $P_Q$ ,  $W$ ,  $B$  and  $a$  in Eq. 6.

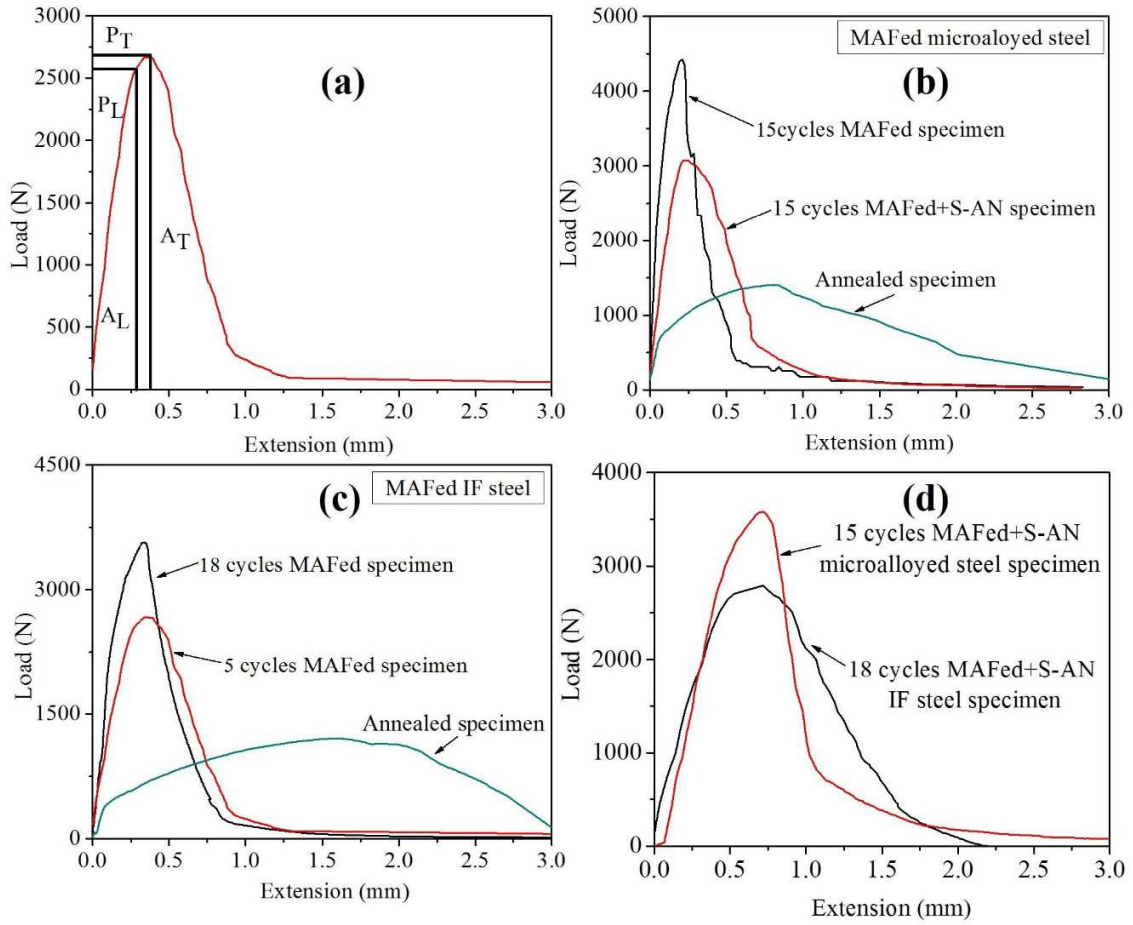


Fig. 16: (a) Estimation of the equivalent load ( $P_Q$  and  $P_E$ ) from the load-extension plot of selected the 5cycles MAFed IF steel sample, (b,c) Load-extension plots of MAFed microalloyed and IF steel specimens, respectively, (d) Load-extension plots of MAFed+short annealed microalloyed and IF steel specimens, respectively.

Similar way, the value of  $K_Q$  for the other selected samples have been evaluated and tabulated in Table 5. Now, in order to check the applicability of the single edge bend test, the experimentally obtained value of  $K_Q$  and yield strength, were replaced in Eq. 7 and it was seen that the values of  $B$  for all the specimens are higher than the actual thickness as well as crack length of the corresponding specimen. Hence, it can be conclude that value of  $K_Q$  obtained from single edge bend test using linear elastic fracture mechanics (LEFM) could not fulfil the validity requirement.

In this regard, further we have chosen another method to estimate the equivalent energy fracture toughness ( $K_{ee}$ ) as per ASTM standard E 992, using the following equations (Eq. 8 and 9) as follows [19, 41].

$$K_{ee} = \frac{P_E S}{B W^{3/2}} \left[ 3 \left( \frac{a}{W} \right)^{\frac{1}{2}} \frac{1.99 - \frac{a}{W} \left( 1 - \frac{a}{W} \left( 2.15 - 3.93 \frac{a}{W} + 2.7 \frac{a^2}{W^2} \right) \right)}{2 \left( 1 + 2 \frac{a}{W} \right) \left( 1 - \frac{a}{W} \right)^{3/2}} \right] \quad (8)$$

$$P_E = P_L \sqrt{\frac{A_T}{A_L}} \quad (9)$$

In this method, the equivalent load  $P_E$  needs to be determined instead of provisional load  $P_Q$  as per ASTM standard E 992 [42]. In this regard, first area ( $A_L$ ) and load ( $P_L$ ) up to linear part of the load vs. extension diagram has to be calculated; next, the area ( $A_T$ ) up to maximum load ( $P_T$ ) is determined. Fig. 16a shows the representative load vs. extension plot for the 5 cycles MAFed IF steel sample to estimate the equivalent load,  $P_E$ , used to evaluate equivalent fracture toughness,  $K_{ee}$  (Fig. 16a). In this case,  $A_T = 717\text{N-mm}$ ,  $P_T = 2659\text{N}$ ,  $A_L = 476\text{N-mm}$ ,  $P_L = 2592\text{N}$ . The equivalent load,  $P_E$  is calculated to be 3181N. This value of  $P_E$  is introduced in Eq. 9 and the  $K_{ee}$  for the 5 cycles MAFed IF steel sample has been estimated to be  $83.2\text{MPa}\sqrt{\text{m}}$ . Similarly, for all other samples,  $K_{ee}$  has been determined and represented in Table 5 along with values of  $K_Q$  and  $J$ -integral of the corresponding sample. It is to be noted that generally, the fracture toughness of materials is mainly affected by three factors (i) reduction of critical plastic strain due to pre-strain, (ii) increase in the strength of material by work hardening and (iii) change in the material resistance to fracture. Although the yield strength of the materials could be enhanced through introduction of a large plastic strain by deformation, but it would decrease the fracture toughness of the material due to reduction of its strain hardening response [40]. Moreover, the value of fracture toughness of bulk materials is influenced by origination and propagation of the crack. Hence, two different approaches usually are used to evaluate fracture toughness, i.e., (i) linear elastic fracture mechanics to examine crack initiation (i.e.  $K_Q$ ) and (ii) elastic plastic fracture mechanics to interpret crack propagation (i.e.  $J$ -integral). Hence, fracture toughness property of sub-micron sized materials might be improved through delayed the crack initiation as well as propagation. In this present study, conditional fracture toughness value ( $K_Q$ ) has been calculated by LEFM method, as  $K_{IC}$  (plane strain fracture toughness), demonstrates the crack initiation in linear elastic fracture mechanics. Alternatively, there is an approach to elucidate the crack propagation in elastic plastic fracture mechanics fracture toughness, i.e.  $J$ -integral value [42]. The  $J$ -integral values for the linear elastic and elastic plastic material, would provide the crack initiation and propagation energy respectively, as per elastic plastic fracture

mechanics [44]. Hence, this parameter also has been determined to clarify the relative enhancement of the fracture toughness and relate with other mechanical properties as well as the microstructural features of the corresponding materials [43]. In the present study, the  $J$ -integral values were calculated through the single edge bend test data as per the ASTM standard 1820-15a [45,46] using the following equation:

$$J = \frac{2A}{Bb} \quad (10)$$

where,  $A$  is the area under the load vs. extension curve up to the maximum load,  $b$  is the unbroken ligament ( $b= 3.75$ ) and  $B$  is the sample thickness ( $B=3.75$  mm). The  $J$ -integral Values calculated using the Eq. 6 is tabulated in Table 5. For example,  $J$ -integral value is calculated to be  $91.7\text{kJ/m}^2$  for the 5 cycles MAFed microalloyed steel sample.

Table 5:  $K_Q$ ,  $K_{ee}$  and  $J$ -integral values for the microalloyed steel samples subjected to single phase control multiaxial forging.

Processing condition		$K_Q$ (MPa $\sqrt{\text{m}}$ )	$K_{ee}$ (MPa $\sqrt{\text{m}}$ )	$J$ -integral (kJ/m $^2$ )	Dimple size ( $\mu\text{m}$ )
Microalloyed steel	H-AN sample	27.7	32.7	48.78	22
	5 cycles MAFed at 650°C	58.8	73.7	85.3	11
	15 cycles MAFed at 650°C	78.5	90.0	97.2	1
	15 cycles MAFed at 650°C+S-AN	89.7	101.3	113.9	5
IF steel	H-AN sample	49.3	57.7	69.6	19
	5 cycles MAFed at 650°C	69.7	83.2	91.7	9
	18 cycles MAFed at 650°C	78.3	97.0	109.0	3
	18 cycles MAFed at 650°C+S-AN	93.5	108.6	116.2	7

It is to be noted that the values of  $K_Q$ ,  $K_{ee}$  and  $J$ -integral of the both microalloyed and IF steel specimens are noticed to increase significantly after the multiaxial forging as compared to H-AN specimens. Remarkable improvement of fracture toughness values are observed in case of 15 cycles MAFed microalloyed and 18 cycles IF steel samples as compared to other specimens. The enhancement of the fracture toughness (i.e.  $K_Q$ ,  $K_{ee}$  and  $J$ -integral) is attributed to the formation of ultrafine ferrite sub structure along with fine fragmented  $\text{Fe}_3\text{C}$  particles in the microalloyed



steel and high density of dislocation substructures/sub cells in the IF steel (as shown in Figs. 8a and 11a). The crack initiation/propagation could effectively be blocked by these dislocation cells/substructures and thereby improve the fracture toughness [42].

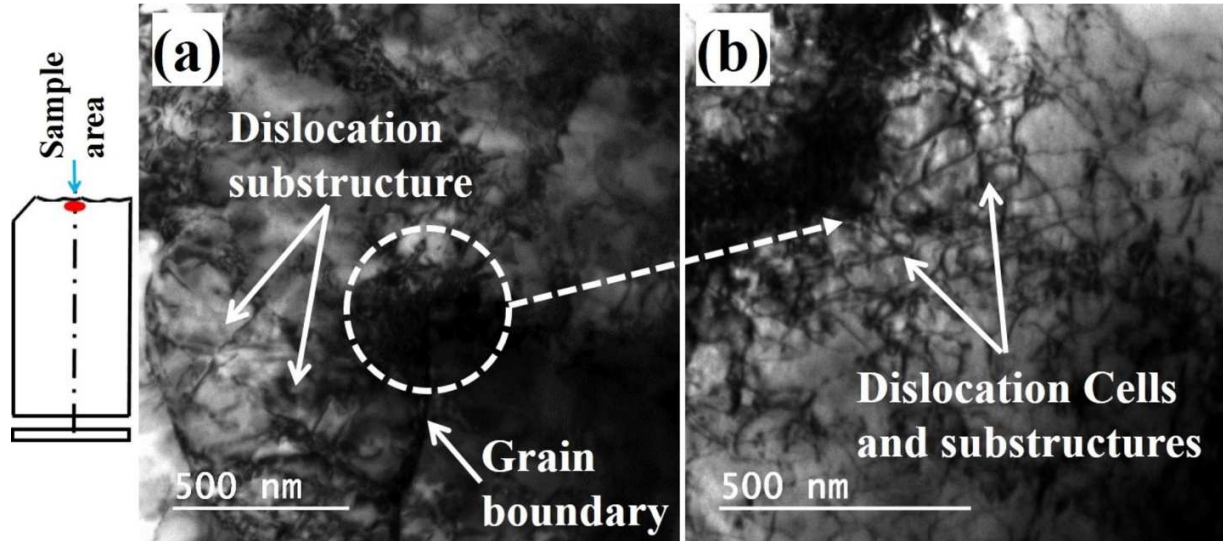


Fig. 17: TEM micrographs of MAFed (a) microalloyed (15 cycles) and (b) IF steel (18 cycles) specimens.

Furthermore, it was noticed that the fracture toughness values (i.e.  $K_{ee}$  and  $J$ ) are higher in case of MAFed+S-AN samples than that of MAFed samples. This endorses further improvement of the fracture toughness of MAFed samples due to the short-annealing treatment. The TEM micrographs near to fractured surface, as shown in Figs. 17a,b also corroborates well with the  $K_{ee}$  and  $J$  values of the corresponding specimens. The fracture toughness parameters i.e.  $K_{ee}$  and  $J$  are more relevant than that of the apparent fracture toughness,  $K_Q$ . This is due to the fact that during the calculation of  $K_{ee}$  and  $J$ , both the load and area under the curve (extension) are taken care; whereas, only the maximum load is used in the calculation of  $K_Q$ . Hence, it can be concluded that the 15/18 cycles MAFed followed by S-AN samples of the microalloyed and IF steels showed better fracture toughness values than that of the other samples. Similar type of fracture behaviour was also observed in the nonferrous materials as reported in the literature [19]. The improvement in the conditional fracture toughness was ascribed to the development of ultrafine sub structure and precipitation of ultrafine carbides. The enhanced fracture toughness has also been stated in other works [7,15,47,48] and the enhancement was ascribed to the development of the ultrafine grain size due to the SPD process.



### 3.5 Fractography analysis

Figs. 18a-f show fractographs of single edge bend tested homogenized annealed, MAFed and MAFed+S-AN microalloyed and IF steel samples. It can be observed from Figs. 18a and b that both the annealed microalloyed and IF steels specimens exhibits ductile failure through developing larger size dimples within the fracture surface. The average dimple size of microalloyed and IF steel specimens are calculated to be  $\sim 22\mu\text{m}$  and  $\sim 29\mu\text{m}$ , respectively (Figs. 19a,b)

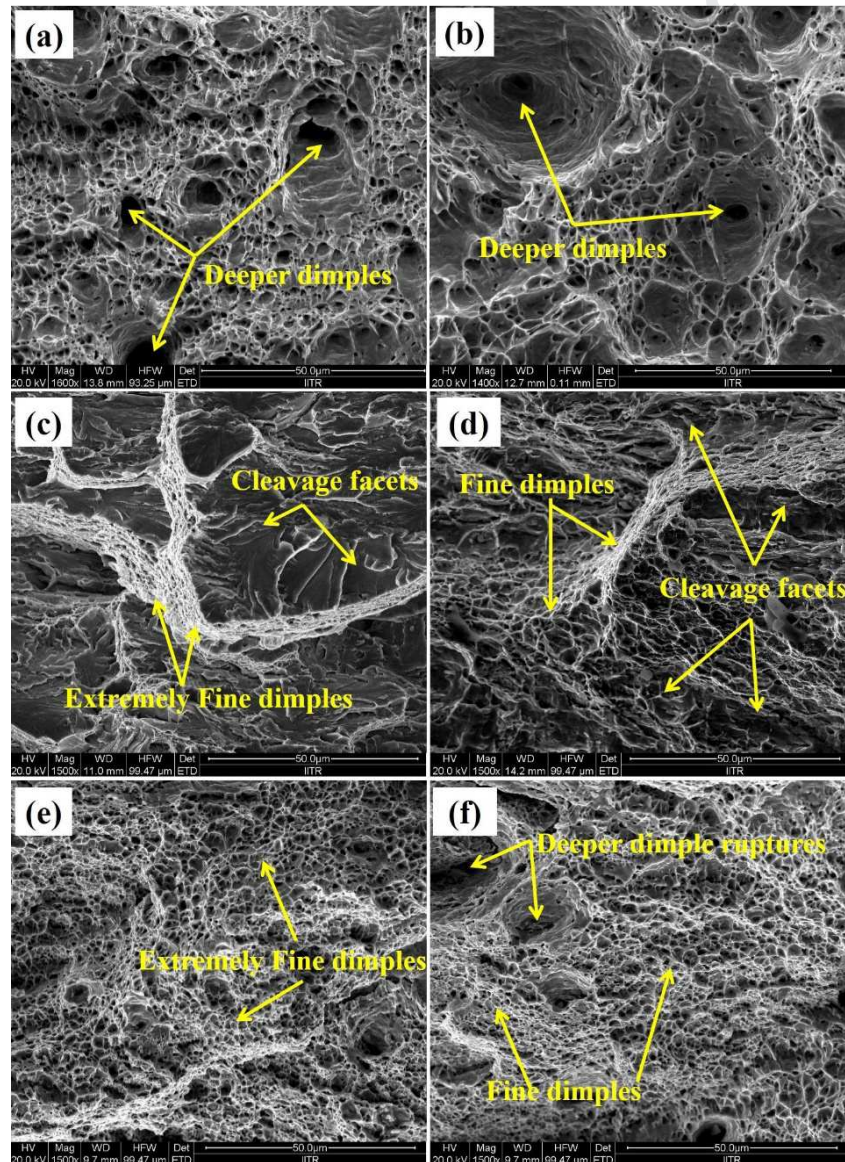


Fig. 18: Fractured surface morphology (a,b) H-AN, (c,d) Single edge bend tested MAFed and (e,f) MAFed+S-AN microalloyed and IF steel specimens, respectively.

The average dimple size reduced to only ~1 and 3  $\mu\text{m}$ , respectively, as shown in Figs. 18c,e and 19a,b for the 15 cycles MAFed microalloyed and 18 cycles MAFed IF steel samples. After the S-AN, the average dimple size increased to ~5 and 7  $\mu\text{m}$ , respectively, in case microalloyed and IF steel specimens (Figs. 18d,f and 19a,b). This indicates partly restoring of the ductility due to the S-AN treatment. The average size of dimples can be linked with the apparent fracture toughness values (Tables 5) of the corresponding specimens. The reduction of the size of dimples during MAF is endorsed to the development of subgrain ferrites as well as dislocation substructures/sub-cells within the ferrite grains; whereas, formation of partially recrystallized ultrafine grains during the S-AN treatment is accountable for the rise in the dimple size of the S-AN samples.

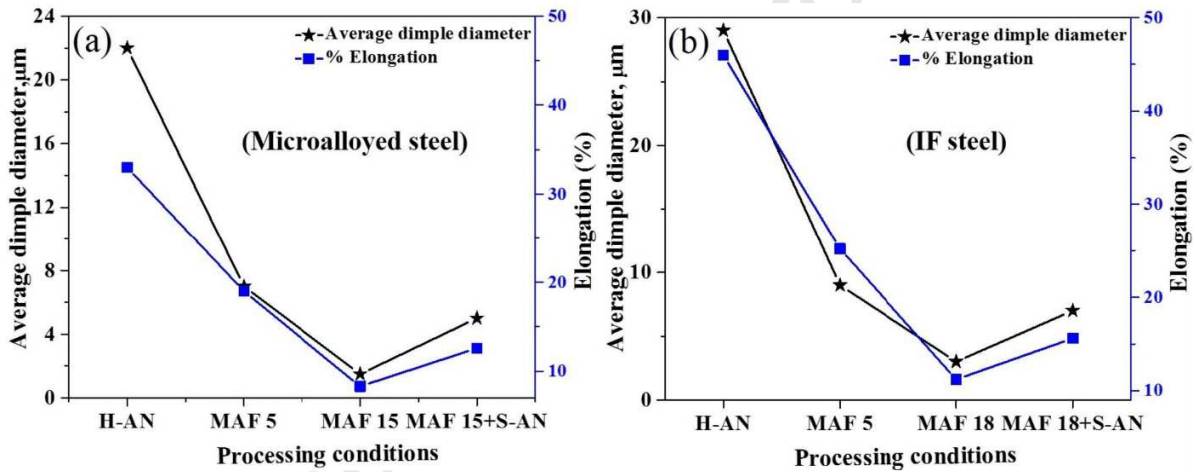


Fig. 19: The average dimple size vs. %elongation of the (a) microalloyed and (b) IF steels samples, respectively, processed at various conditions.

Moreover, the existence of cleavage facets can be found within the fractured surface of both MAFed and MAFed+S-AN microalloyed steel specimens (18c,d). This is ascribed to the occurrence of hard phase i.e. fragmented  $\text{Fe}_3\text{C}$  (as shown in Fig. 6d) within the soft ferrite matrix. Moreover, improvement of the fracture toughness (both  $K_{\text{Ic}}$  and  $J$ -integral values) after MAFed+S-AN could be attributed due to the presence of partially recovered equiaxed subsize grains, formed through the partial recovery and recrystallization of the MAFed specimens during short annealing treatment. Similar types of observation were also stated by numerous researchers in case of the severely deformed nonferrous alloys [19,48].

#### 4. Conclusions

Fracture toughness values of the UFG microalloyed and IF steel specimens have been studied in detail to correlate with the other mechanical properties of the corresponding samples. In this regard, the following points could be concluded as the important outcomes of this study.

- (i) The maximum refinement of grains was accomplished when the multi-axial forging has been carried out up to 15 cycles at  $\alpha+\gamma$  phase regime ( $\sim A_{r1}$ ) in microalloyed steel specimen and up to 18 cycles at pure ferritic ( $\alpha$  phase) regime in IF steel specimens. This is endorsed to the formation of micro-shear bands in multiple directions through alternating change in the accumulated strain paths to endorse dislocation activity and DIFT, and increase in the misorientation angles of grain boundaries. This has been confirmed by TEM and EBSD investigation.
- (ii) More than 4-fold enhancement of the YS (1027 MPa) of the MAFed (15 cycles at 650°C) microalloyed steel as compared to that of the starting sample (251 MPa) is ascribed to the development of submicron size ( $\sim 280$  nm) ferrite grains (obtained through grain subdivision and recovery) and formation of nanosize (35 nm) fragmented cementite (precipitated through repeated heating cycles) within the ultrafine ferrite matrix. On the other hand almost 6 times enhancement of the YS (881 MPa) of the MAFed (18 cycles at 650°C) IF steel as compared to that of the starting sample (141 MPa) is attributed to the formation of submicron size ferrite grain ( $\sim 320$  nm) along with high density of dislocation substructures.
- (iii) In both cases the best combination of the YS and ductility (YS=949 MPa, %El.=12.6 for microalloyed and YS=817 MPa, %El.=15.6 for IF steel) of the MAFed+S-AN specimen is ascribed to the partial recovery of the subgrains and dislocation annihilations during the short-annealing treatment.
- (iv) Fracture toughness analysis was made for the selected specimens through 3-point bend test results. The 15 cycles MAFed microalloyed steel specimen showed superior fracture toughness ( $K_{Ic}=90.0 \text{ MPa}\sqrt{\text{m}}$ ) along with high YS (1027 MPa) and significant amount of ductility (%El.=8.3); whereas, the best combination of YS (881 MPa), ductility (%El.=11.2) and fracture toughness ( $K_{Ic}=97.0 \text{ MPa}\sqrt{\text{m}}$ ) has been achieved for the 18 cycles MAFed IF steel samples. The improved mechanical properties are ascribed to the

formation of ultrafine subgrains and nanosize (35nm)  $\text{Fe}_3\text{C}$  particles (in case of microalloyed steel), distributed homogeneously throughout the microstructure in the MAFed samples.

- (v) Calculation of fracture toughness value through EPFM method ( $J$ -integral) is acceptable to estimate the fracture toughness values by single edge bend test as it considers the total area under the load vs. extension plot. Moreover, EPFM concept might construe crack propagation mechanisms. Furthermore, estimation of fracture toughness through equivalent energy ( $K_{ee}$ ) approach is also suitable as it considers the maximum load as well as area up to the linear extension under single point edge test to estimate its value. Both the methods could estimate the convincing fracture toughness values when it is challenging to determine plain strain fracture toughness ( $K_{IC}$ ) of the sample.

#### Data availability statement

All data comprised in the current study are available upon request by communicating the corresponding author.

#### Acknowledgement

The authors are highly acknowledged Metallurgical and Materials Engineering Department, IIT Roorkee for offering the research facilities to carry out the current research work.

#### References

- [1] Morrison WB. Microalloy steels-the beginning. *Mater Sci Technol* 2009; 25:1066-1073.
- [2] Misra RDK, Nathani H, Hartmann JE, Siciliano F. Microstructural evolution in a new 770 MPa hot rolled Nb-Ti microalloyed steel. *Mater Sci Eng A* 2005; 394:339-352.
- [3] Azushima A, Kopp R, Korhonen A, Yang DY, Micari F, Lahoti GD, Groche P, Yanagimoto J, Tsuji N, Rosochowski A, Yanagida A. Severe plastic deformation (SPD) processes for metals. *CIRP Ann Manuf Technol* 2008;57:716-735.
- [4] Alexander DJ. New Methods for Severe Plastic Deformation Processing. *J Mater Eng Perform* 2007;16:360-374.
- [5] Verma D, Mukhopadhyay NK, Sastry GVS, Manna R. Ultra-High-Strength Interstitial-Free Steel Processed by Equal-Channel Angular Pressing at Large Equivalent Strain. *Metal Mater Trans A* 2016; 47:1803-1817.
- [6] Kim J, Kim I, Shin DH. Development of deformation structures in low carbon steel by equal channel angular pressing. *Scripta Mater* 2001;45:421-426.
- [7] Singh RB, Mukhopadhyay NK, Sastry GVS, Manna R. Development of High-Strength Bulk Ultrafine-Grained Low Carbon Steel Produced by Equal-Channel Angular Pressing. *Metal Mater Trans A* 2017;48:5449-5466.
- [8] Song R, Ponge D, Raabe D, Speer JG, Matlock DK. Overview of processing, microstructure and mechanical properties of ultrafine grained bcc steels. *Mater Sci Eng A* 2006;441:1-17.



- [9] Halfa H. Recent trends in producing ultrafine grained steels. *Journal of Minerals and Mater. Charact Eng* 2014;2:428-469.
- [10] Lim SM, Wahabi ME, Desrayaud C, Montheillet F. Microstructural refinement of an Fe–C alloy within the ferritic range via two different strain paths. *Mater Sci Eng A* 2007;532:460-461.
- [11] Wang YB, Ho JC, Liao XZ, Li HQ, Ringer SP, Zhu YT, Mechanism of grain growth during severe plastic deformation of a nanocrystalline Ni–Fe alloy, *Appl Phys Lett* 2009;94:011908.
- [12] Li JCM, Mechanical Grain Growth in Nanocrystalline Copper, *Phys Rev Lett* 2006;96:215506.
- [13] Bhowmik A, Biswas S, Dhinwal SS, Sarkar A, Ray RK, Bhattacharjee D, Suwas S. Microstructure and texture evolution in interstitial-free (IF) steel processed by multi-axial forging. *Mater. Sci. Forum* 2012;702-703:774-777.
- [14] Han BJ, Xu Z. Microstructure evolution mechanism of Fe-Ni alloy during severe plastic deformation. *J Iron and Steel Res* 2009;21:31-36.
- [15] Belyakov A, Tsuzaki K, Miura H, Sakai T. Effect of initial microstructures on grain refinement in a stainless steel by large strain deformation. *Acta Materialia* 2003;51:847-861.
- [16] Kundu A, Kapoor R, Tewari R, Chakravartty JK. Severe plastic deformation of copper using multiple compression in a channel die. *Scripta Mater* 2008;58:235-238.
- [17] Hohenwarter A, Pippan R. Fracture toughness evaluation of ultrafine-grained nickel. *Scr Mater* 2011;64:982-985.
- [18] Dasharath SM, Mula S. Improvement of mechanical properties and fracture toughness of low SFE Cu-Al alloy through microstructural modification by multiaxial cryoforging. *Mater Sci Eng A* 2017;690:393-404.
- [19] Joshi A, Kumar N, Yogesha KK, Jayaganthan R, Nath SK. Mechanical properties and microstructural evolution in Al 2014 alloy processed through multidirectional cryoforging. *J Mater Eng Perform* 2016;25:3031-3045.
- [20] Toulfatzis AI, Pantazopoulos GA, Paipetis AS. Fracture behavior and characterization of lead-free, brass alloys for machining applications. *J Mater Eng Perform* 2014;23:3193-3206.
- [21] Kapoor R, Sarkar A, Yogi R, Shekhawat SK, Samajdar I, Chakravartty JK. Softening of Al during multi-axial forging in a channel die. *Mater Sci Eng A* 2013;560:404-412.
- [22] Shrivastava S, Ghosh C, Jonas JJ. A comparison of the von Mises and Hencky equivalent strains for use in simple shear experiments. *Phil Mag A* 2012;92:779-786.
- [23] Onaka S. Comment on “A comparison of the von Mises and Hencky equivalent strains for use in simple shear experiments”. *Phil Mag A* 2012;92:2264-2271.
- [24] Segal VM. Equivalent and effective strains during severe plastic deformation (SPD), *Phil Mag Lett* 2018;98:511-520.
- [25] Hu J, Du LX, Xie H, Gao XH, Misra RDK. Microstructure and mechanical properties of TMCP heavy plate microalloyed steel. *Mater Sci Eng A* 2014;607:122-131.
- [26] Ghosh S, Singh AK, Mula S, Chanda P, Mahashabde VV, Roy TK. Mechanical properties, formability and corrosion resistance of thermomechanically controlled processed Ti-Nb stabilized IF steel. *Mater Sci Eng A* 2017; 684:22-36.
- [27] Ghosh S, Singh AK, Mula S. Effect of critical temperatures on microstructures and mechanical properties of Nb-Ti stabilized IF steel processed by multiaxial forging. *Mater Des* 2016;100:47-57.
- [28] Sun ZQ, Yang WY, Ji QQ. Deformation enhanced transformation and dynamic recrystallization of ferrite in a low carbon steel during multipass deformation. *Mater Sci Eng A* 2002;334:201-206.
- [29] Zhao B, Liu F, Li G, Xu R, Yang J. Effect of temperature and strain on microstructure refinement in low carbon microalloyed steel during multi-axis deformation process. *Metals and Materials Int* 2013;19:549-553.
- [30] Raghavan V. *Materials Science and Engineering*, 5th Edition, PHI Learning, 2004, 225-400.

- [31] Bodin A, Sietsma J, van der ZS. On the nature of the bimodal grain size distribution after intercritical deformation of a carbon-manganese steel. *Mater Charact* 2001;47:187-193.
- [32] Cízek J, Janecek M, Krajnak T, Straska J, Hruska P, Gubicza J, Kim H.S. Structural characterization of ultrafine-grained interstitial-free steel prepared by severe plastic deformation. *Acta Mater* 2016;105:258-272.
- [33] Ungar T, Ott S, Sanders PG, Borbely A, Weertman JR. Dislocations, grain size and planar faults in nanostructured copper determined by high resolution X-ray diffraction and a new procedure of peak profile analysis. *Acta. Mater.* 1998;46:3693-3699.
- [34] Mote VD, Purushotham Y, Dole BN. Williamson-Hall analysis in estimation of lattice strain in nanometer-sized ZnO particles. *J. Theo. Appl. Phys.* 2012;6:1-8.
- [35] Dieter GE. Evaluation of workability, *Metals Handbook*, 9th Edition, 14, American Society of Metals, Metals Park, OH, 1988, 363-372.
- [36] Zhao YH, Horita Z, Langdon TG, Zhu YT. Evolution of defect structures during cold rolling of ultrafine-grained Cu and Cu–Zn alloys: Influence of stacking fault energy. *Mater. Sci. Eng. A* 2008;474:342-347.
- [37] Sarkar A, Bhowmik A, Suwas S. Microstructural characterization of ultrafine-grain interstitial-free steel by X-ray diffraction line profile analysis. *Appl. Phys. A* 2009;94:943-948.
- [38] Hu J, Du LX, Xie H, Gao XH, Misra RDK. Microstructure and mechanical properties of TMCP heavy plate microalloyed steel. *Mater. Sci. Eng. A* 2014;607:122-131.
- [39] Kang DH, Kim DW, Kim S, Bae GT, Kim KH, Kim NJ. Relationship between stretch formability and work-hardening capacity of twin-roll cast Mg alloys at room temperature. *Scr. Mater.* 2009;61:768-771.
- [40] Banks-Sills L, Dunye I. A note on the effect of plastic strain on fracture toughness. *Eng. Frac. Mech.* 1997;57:67-73.
- [41] Tochaee EB, Hosseini HRM, Reihani SMS. On the fracture toughness behavior of in-situ Al–Ti composites produced via mechanical alloying and hot extrusion. *J Alloy Compd* 2016;681:12-21.
- [42] Zhu, XK, Joyce JA. Review of fracture toughness (G, K, J, CTOD, CTOA) testing and standardization. *Eng Fract Mech* 2012;85:1-46.
- [43] Broek D. *Elementary Engineering Fracture Mechanics*, 3rd edition, Springer, Berlin, 2012, 24-66.
- [44] Rice JR. A path independent integral and the approximate analysis of strain concentration by notches and cracks. *J Appl Mech* 1968;35:379-386.
- [45] Gdoutos EE. *Fracture Mechanics: An introduction*, 2nd edition, Springer, Berlin, 2006, 1-238.
- [46] Donato GHB, Ruggieri C. Estimation procedures for J and CTOD fracture parameters using three-point bend specimens. *Proc. Intern. Pipeline Conf* 2006:149-157.
- [47] Jha AK, Sreekumar K, Tharian T, Sinha PP. Process optimization for high fracture toughness of maraging steel rings formed by mandrel forging. *J Manuf Process* 2010;12:38-44.
- [48] Zhang Z, Jing H, Xu L, Han Y, Zhao L, Lv X, Zhang J. The impact of annealing temperature on improving microstructure and toughness of electron beam welded duplex stainless steel, *J Manuf Process* 2018;31:568-582.

## Figure captions

Fig. 1: Representation of multiaxial forging schedule for one cycle.

Fig. 2: (a) Schematic presentation of a single edge bend specimen, (b) micrograph of single edge bend specimen.

Fig. 3: Optical microstructure of homogenized annealed (a) microalloyed and (b) IF steel specimens.

Fig. 4: (a) EBSD inverse pole figure map, (b) magnified image of the selected location as indicated using dotted line in Fig. 4a, (c) grain boundary map (d) grain average misorientation map of  $\alpha+\gamma$  region

- control 5 cycles MAFed microalloyed steel specimen, (e and f) misorientation profile and grain size distribution of corresponding specimen, respectively.
- Fig. 5: (a) EBSD inverse pole figure map, (b) grain boundary map of 15 cycles MAFed microalloyed steel specimen, (c and d) misorientation profile and grain size distribution of corresponding specimen, respectively.
- Fig. 6: SEM micrograph of (a) annealed, (b) magnified image Fig. 6a, (c) 5cycles and (d) 15cycles MAFed microalloyed steel (at  $\sim A_{r1}$ ) and (e) EDAX analysis on selected spot of the corresponding specimens.
- Fig. 7: (a) EBSD inverse pole figure map, (b) grain boundary map of 15 cycles MAFed+S-AN microalloyed steel specimen, (c and d) misorientation profile and grain size distribution of corresponding specimen, respectively.
- Fig. 8: TEM bright field image of microalloyed steel specimens: (a) MAFed (15 cycles) at  $\sim A_{r1}$  region and (b) MAFed (15 cycles)+S-AN.
- Fig. 9: (a,c) EBSD inverse pole figure map, (b,d) grain boundary map of 18cycles MAFed and MAFed+S-AN IF steel specimens, respectively, (c and d) misorientation profile and grain size distribution of corresponding specimen, respectively.
- Fig. 10: (a,c) EBSD inverse pole figure map, (b,d) grain boundary map of 18cycles MAFed and MAFed+S-AN IF steel specimens, respectively, (c and d) misorientation profile and grain size distribution of corresponding specimen, respectively.
- Fig. 11: TEM bright field image of IF steel specimens: (a) MAFed for 18 cycles at  $\alpha$  region and (b) MAFed (18 cycles)+S-AN.
- Fig. 12: Tensile stress-strain curves of MAFed (a) microalloyed and (b) IF steel specimens.
- Fig. 13: X-ray diffraction pattern of the (a) MAFed microalloyed and (b) IF steels specimens at different processing conditions.
- Fig. 14: (a,b) strain hardening rate vs. true stress curves of multiaxially forged microalloyed and IF steels at different processing conditions.
- Fig. 15: Variation of Uniform elongation (UE) and yield strength (YS) and with strain hardening exponent ( $n$ ).
- Fig. 16: (a) Estimation of the equivalent load (PQ and PE) from the load-extension plot of selected the 5cycles MAFed IF steel sample, (b,c) Load-extension plots of MAFed microalloyed and IF steel specimens, respectively, (d) Load-extension plots of MAFed+short annealed microalloyed and IF steel specimens, respectively.
- Fig. 17: TEM micrographs of MAFed (a) microalloyed (15 cycles) and (b) IF steel (18 cycles) specimens.
- Fig. 18: Fractured surface morphology (a,b) H-AN, (c,d) Single edge bend tested MAFed and (e,f) MAFed+S-AN microalloyed and IF steel specimens, respectively.
- Fig. 19: The average dimple size vs. %elongation of the (a) microalloyed and (b) IF steels samples, respectively, processed at various conditions.

## Table captions

- Table 1: Chemical composition (wt. %) of the low C microalloyed and IF steels.
- Table 2: The Mechanical properties of the Homogenized annealed (H-AN) and MAFed microalloyed and IF steel specimens.
- Table 3: Lattice microstrain, crystallite size and amount of dislocation density, predicted and experimentally obtained YS for MAFed IF steel at different conditions.
- Table 4: Lattice microstrain, crystallite size and amount of dislocation density, predicted and experimentally obtained YS for MAFed microalloyed steel at different conditions.
- Table 5:  $K_Q$ ,  $K_{ec}$  and J-integral values for the microalloyed steel samples subjected to single phase control multiaxial forging.

**Research Highlights**

- UFG microalloyed and IF steels produced through phase control multiaxial forging.
- Mechanism of UFG formation analyzed in light of DIFT/DRX mechanisms.
- Analyzed the fracture toughness through computing  $K_Q$ , J-integral and  $K_{ee}$  values.
- Quantitative measurements grain size/distribution investigated through EBSD/TEM.
- Nano size  $Fe_3C$  effectively block the crack initiation/propagation.



**Declaration of interests**

☒ The authors declare that they have no known competing financial interests or personal relationships that could have appeared to influence the work reported in this paper.

☐ The authors declare the following financial interests/personal relationships which may be considered as potential competing interests: